Received: 24 February 2017 | Revised: 30 August 2017 | Accepted: 3 September 2017

DOI: 10.1002/nag.2748

RESEARCH ARTICLE

WILEY

A two-phase SPH model for debris flow propagation

M. Pastor[1] | A. Yague[1] | M.M. Stickle[1] | D. Manzanal[1] | P. Mira[2]

[1] Department of Applied Mathematics, ETS Ingenieros de Caminos, Universidad Politécnica de Madrid, Spain

[2] Laboratorio de Geotecnia, Centro de Estudios y Experimentación de Obras Públicas (CEDEX), 28014 Madrid, Spain

Correspondence
Manuel Pastor, Department of Applied Mathematics, ETS Ingenieros de Caminos, Universidad Politécnica de Madrid, Calle del Profesor Aranguren, 3, 28040 Madrid Spain.
Email: manuel.pastor@upm.es

Summary

This paper presents a model which can be used for fast landslides where coupling between solid and pore fluid plays a fundamental role. The proposed model is able to describe debris flows where the difference of velocities between solid grains and fluid is important. The approach is based on the mathematical model proposed by Zienkiewicz and Shiomi, which is similar to those of Pitman and Le and Pudasaini. The novelty of the present work is the numerical technique used, the smoothed particle hydrodynamics (SPH). We propose to use a double set of nodes for soil and water phases, the interaction between them being described by a suitable drag law. The paper presents both mathematical and numerical models, describing the main assumptions and their limitations. Then, the model is applied to (1) a simple case where shocks and expansion waves appear, (2) a dam break problem on a horizontal plane with a frictional soil phase, and (3) a debris flow which happened in Hong Kong. The main conclusions that can be drawn from the applications are:

(i) Debris flows having 2 phases with important relative mobility present a rich structure of shocks and rarefaction waves, which has to be properly modeled. Otherwise, the model will have numerical damping or dispersion.
(ii) Dambreak exercises provide interesting information in simple and controlled situations. We can see how both phases move relative to each other.
(iii) Real debris flows can be simulated with the proposed model, obtaining reasonable results.

KEYWORDS

debris flow, landslide propagation, mathematical model, SPH

1 | INTRODUCTION

The term "landslide" embraces a large variety of phenomena. According to Dikau,[4] there are 2 main groups of landslides referred to as slides and flows. The most interesting difference, from a geomechanical point of view, is that slides present a failure surface while flows usually present a diffuse failure mechanism, with shear strains distributed along most of the mass. Regarding flow type movements, we find rock avalanches, debris flows, mudflows, and flow slides.

In the case of rock avalanches, the flowing material consists on solid blocks which are disintegrating into smaller particles as it propagates downhill. Segregation is also present, the larger blocks traveling at the front and on the upper part. Discrete element models are able to describe both phenomena, but the computational cost of representing a real

case is still too large. This is the reason why continuum models are frequently applied here, using a single-phase granular fluid.

Mudflows consist of mixtures of fine soil particles and water, and they can be modeled with continuum models using a single-phase viscous fluid.

Flowslides are mixtures of soil particles and water, with small relative displacements between both phases. The tendency of the solid skeleton to dilate or contract results on pore pressure generation affecting the effective stresses. To describe them, mathematical models formulated in terms of velocities and pore pressures, like the $\boldsymbol{u}-p_w$ model proposed in Zienkiewicz and Shiomi,[1] provide a good approximation. According to Hutchinson,[5] *"...they present the essential feature that the material involved has a metastable, loose or high porosity structure. ...This structure collapses transferring the overburden load wholly or partially onto the pore fluid in which excess pressures are generated."*

Debris flows are the more complex phenomenon from the modeling point of view, as both solid particles and water can have different velocities. The models have to include velocities of both solid and fluid phases, and the stresses acting on them.

This paper is devoted to the case of debris flows, where both phases and their mutual interaction have to be modeled. While models for debris flows are relatively modern in engineering geology, their origin can be tracked back along 2 different paths:

(i) Zienkiewicz, following Biot,[6,7] proposed a general formulation which can be applied to debris flows.[1] From here, simpler approximations such as the $u-p_w$ model were derived. This model is used today in most of coupled problems of geotechnical engineering.

(ii) Within the area of physics of granular media, where important contributions have been made to study industrial problems such as the fluidized beds, it is worth mentioning the work done by Bowen,[8] Anderson and Jackson.[9] Regarding applications to debris flows, Pitman and Le[2] and Pudasaini[3] have proposed 2-phase models for debris flows, arriving to most interesting 2-phase simplified models of depth integrated type.

In the same manner than the general 2-phase model of Zienkiewicz and Shiomi[1] can be particularized to the $\boldsymbol{u}-p_w$ model, depth integrated models based on this approach have been proposed by Iverson and Denlinger[10] and Pastor and co-workers.[11,12]

In Pitman and Le[2], it is stated that triggering is different from propagation and has to be modeled using a different approach, their model being applied only to propagation. However, in the authors' opinion, the same mathematical model can be applied to initiation and propagation, the key being the constitutive model describing the behavior of the material, from solid to fluidized states.

This problem has attracted the attention of researchers during past years. Prime and co-workers[13] have proposed to use an indicator of fluidization to change from a solid model to a Bingham fluid. Berzi and co-workers[14] have investigated the case of granular fluids. Finally, the authors have proposed the use of viscoplasticity for both situations.[15,16]

Regarding numerical models, there are nowadays some interesting approaches that could be used, for example, the smooth particle hydrodynamics (SPH) and the material point model (MPM). The authors have explored the former approach in Blanc and Pastor,[17,18] finding that features such as coupling with pore water and failure mechanisms can be accurately described. Both MPM and SPH are lagrangian approaches. They present, in comparison to the eulerian approaches, the advantage of not needing special techniques such as level set to track interfaces.[19-21]

In the case of depth integrated models, both approaches can be used. So far, most of the models are of eulerian type[2,3,11] using finite volumes or elements or of lagrangian type (SPH).[12,22,23]

In a previous publication, the authors have addressed the problem of coupling SPH with a series of finite difference (FD) meshes associated to each SPH node, which provides better accuracy to reproduce pore pressure changes.[15]

Here, we will model debris flows using 2 sets of nodes, describing the water and the solid phases, which can move relative to each other.

The paper is structured as follows:

(i) We will present first the mathematical model which will be used, deriving it from Zienkiewicz-Shiomi model,[1] and arriving to the depth integrated model proposed by Pitman and Le.[2]

(ii) Next, the SPH model for 2 phases will be described.

(iii) Finally, we will present some application cases where we will compare the results provided by the proposed model against those obtained using more simplified models.

2 | MATHEMATICAL MODEL

2.1 | Introduction

We will assume that the debris flow material is a saturated 2-phase mixture, where the solid phase consists of solid particles of different sizes and the fluid phase is either water, or a mixture of water with very fine soil particles such as clay, which can be considered as a fluid. We will denote them by the sub indexes s and w. Densities will be denoted as ρ_s and ρ_w. The mixture is described using its porosity n (volume fraction of voids in the mixture), the void ratio e being related to the porosity by

$$n = \frac{e}{1+e} \tag{1}$$

We will introduce the concept of phase densities as the mass of components per unit volume of mixture, which are given by

$$\begin{aligned} \rho^{(s)} &= (1-n)\rho_s \\ \rho^{(w)} &= n\rho_w \end{aligned} \tag{2}$$

One important feature of debris flows is that velocities of both phases can be different. Therefore, the mathematical models describing the balance of mass and momentum for both phases use derivatives following the solid $\frac{d^{(s)}}{dt}$ and the fluid $\frac{d^{(w)}}{dt}$ defined by

$$\begin{aligned} \frac{d^{(s)}}{dt} &= \frac{\partial}{\partial t} + \boldsymbol{v}_s{}^T.\,\mathrm{grad} \\ \frac{d^{(w)}}{dt} &= \frac{\partial}{\partial t} + \boldsymbol{v}_w{}^T.\,\mathrm{grad} \end{aligned} \tag{3}$$

where $\boldsymbol{v}_s$ and $\boldsymbol{v}_w$ are the velocities of solid and fluid particles in the mixture. Both derivatives are related by

$$\frac{d^{(w)}}{dt} = \frac{d^{(s)}}{dt} + (\boldsymbol{v}_w - \boldsymbol{v}_s)^T.\,\mathrm{grad} \tag{4}$$

In classical Soil Mechanics, where relative velocities are small, a lagrangian framework is used for the solid, the velocity of the fluid relative to the skeleton given by the Darcy's velocity $\boldsymbol{w}$ defined as

$$\boldsymbol{v}_w = \boldsymbol{v}_s + \frac{\boldsymbol{w}}{n} \tag{5}$$

from which we arrive to

$$\frac{d^{(w)}}{dt} = \frac{d^{(s)}}{dt} + \frac{\boldsymbol{w}^T}{n}.\,\mathrm{grad} \tag{6}$$

Regarding the stresses, the total stress in the mixture (Cauchy) is denoted by $\boldsymbol{\sigma}$ and is related to stresses in the phases as

$$\begin{aligned} \boldsymbol{\sigma} &= (1-n)\,\boldsymbol{\sigma}_s + n\boldsymbol{\sigma}_w \\ &= \boldsymbol{\sigma}^{(s)} + \boldsymbol{\sigma}^{(w)} \end{aligned} \tag{7}$$

where the partial stresses $\boldsymbol{\sigma}^{(s)}$ and $\boldsymbol{\sigma}^{(w)}$ have been introduced as

$$\begin{aligned} \boldsymbol{\sigma}^{(s)} &= (1-n)\,\boldsymbol{\sigma}_s \\ \boldsymbol{\sigma}^{(w)} &= n\boldsymbol{\sigma}_w \end{aligned} \tag{8}$$

Partial stresses are a decomposition of the stress tensor into the stress which is carried by both phases. They provide a complementary explanation to the magnitudes used in geotechnical engineering, their range of application being larger.[2,8,9,24]

The stress in the fluid phase can be written as:

$$\boldsymbol{\sigma}^{(w)} = -np_w\boldsymbol{I} + n\boldsymbol{s}_w \tag{9}$$

where $\boldsymbol{s}_w$ is the deviatoric stress, p_w the pore pressure, and $\boldsymbol{I}$ the second-order identity tensor. From here, the total stress is:

$$\boldsymbol{\sigma} = \boldsymbol{\sigma}^{(s)} - np_w\boldsymbol{I} + n\boldsymbol{s}_w \tag{10}$$

In the case of an inviscid pore fluid, we can express the effective stress used in geotechnical engineering as:

$$\boldsymbol{\sigma}' = \boldsymbol{\sigma} + p_w\boldsymbol{I} \tag{11}$$

which can be written as:

$$\boldsymbol{\sigma}' = (1-n)(\boldsymbol{\sigma}_s + p_w\boldsymbol{I}) \tag{12}$$

In the present work, compression is assumed negative. The effective stress is related to the solid partial stress by:

$$\boldsymbol{\sigma}^{(s)} = \boldsymbol{\sigma}' - (1-n)p_w\boldsymbol{I} \tag{13}$$

If we define the effective component stress as $\boldsymbol{\sigma}^{eff} = (\boldsymbol{\sigma}_s + p_w\boldsymbol{I})$, we arrive to:

$$\boldsymbol{\sigma}' = (1-n)\boldsymbol{\sigma}^{eff} \tag{14}$$

The effective stress in the more general case of a viscous porous fluid is:

$$\boldsymbol{\sigma}' = \boldsymbol{\sigma} + p_w\boldsymbol{I} - n\boldsymbol{s}_w \tag{15}$$

2.2 | Balance of mass and momentum

The **balance of mass** equations are given by

$$\begin{aligned} &\frac{d^{(s)}}{dt}((1-n)\rho_s) + (1-n)\rho_s \operatorname{div}\boldsymbol{v}_s = 0 \\ &\frac{d^{(w)}}{dt}(n\rho_w) + n\rho_w \operatorname{div}\boldsymbol{v}_w = 0 \end{aligned} \tag{16}$$

which can be written as:

$$\begin{aligned} &(1-n)\frac{1}{\rho_s}\frac{d^{(s)}\rho_s}{dt} - \frac{d^{(s)}n}{dt} + (1-n)\operatorname{div}\boldsymbol{v}_s = 0 \\ &n\frac{1}{\rho_w}\frac{d^{(w)}\rho_w}{dt} + \frac{d^{(w)}n}{dt} + n\operatorname{div}\boldsymbol{v}_w = 0 \end{aligned} \tag{17}$$

If we consider both the fluid and the solid grains as elastic, with volumetric deformations induced only by the fluid pressure p_w, then the volumetric stiffness moduli K_s and K_w can be introduced by

$$\frac{1}{\rho_s}\frac{d^{(s)}\rho_s}{dt} = \frac{1}{K_s}\frac{d^{(s)}p_w}{dt}$$
$$\frac{1}{\rho_w}\frac{d^{(w)}\rho_w}{dt} = \frac{1}{K_w}\frac{d^{(w)}p_w}{dt} \tag{18}$$

Taking into account 18 and combining equations in 17, the following expression is obtained

$$\frac{(1-n)d^{(s)}p_w}{K_s\ dt} + \frac{n}{K_w}\frac{d^{(w)}p_w}{dt} + \frac{d^{(w)}n}{dt} - \frac{d^{(s)}n}{dt} + (1-n)\,\mathrm{div}\,\boldsymbol{v}_s + n\,\mathrm{div}\,\boldsymbol{v}_w = 0 \tag{19}$$

and taking 6 into account the following mixture balance of mass is derived:

$$\frac{(1-n)d^{(s)}p_w}{K_s\ dt} + \frac{n}{K_w}\frac{d^{(w)}p_w}{dt} + \mathrm{div}\,\boldsymbol{w} + \mathrm{div}\,\boldsymbol{v}_s = 0 \tag{20}$$

If solid grains are considered much stiffer than pore fluid, then the first term in 20 can be neglected arriving to

$$\frac{n}{K_w}\frac{d^{(w)}p_w}{dt} + \mathrm{div}\,\boldsymbol{w} + \mathrm{div}\,\boldsymbol{v}_s = 0 \tag{21}$$

For simplicity,[1,24] a mixed volumetric stiffness Q can be introduced as:

$$\frac{1}{Q} = \frac{(1-n)}{K_s} + \frac{n}{K_w} \approx \frac{n}{K_w} \tag{22}$$

In the case where the solid grains are much stiffer than pore fluid, the mass balance equation for the solid phase reads:

$$-\frac{d^{(s)}n}{dt} + (1-n)\,\mathrm{div}\,\boldsymbol{v}_s = 0 \tag{23}$$

These aspects are described in detail in Zienkiewicz et al[24] and Lewis and Schrefler.[25]

Concerning **balance of momentum equations**, the form proposed by Zienkiewicz and Shiomi[1] in 1984 for inviscid pore fluids derives from:

$$(1-n)\rho_s\frac{d^{(s)}\boldsymbol{v}_s}{dt} = \mathrm{div}\,\boldsymbol{\sigma}' - (1-n)\,\mathrm{grad}\,(p_w) + (1-n)\rho_s\boldsymbol{b} + (1-n)\boldsymbol{R}_s \tag{24}$$

$$n\rho_w\frac{d^{(w)}\boldsymbol{v}_w}{dt} = -n\,\mathrm{grad}\,p_w + n\rho_w\boldsymbol{b} + n\boldsymbol{R}_w \tag{25}$$

where:

$\boldsymbol{b}$ is the body forces vector

$\boldsymbol{R}_s$ and $\boldsymbol{R}_w$ characterize the interaction between phases: (26)

$$n\boldsymbol{R}_w = -(1-n)\boldsymbol{R}_s = -\boldsymbol{R}$$

Equations 24 and 25 can be written alternatively in terms of either partial or total stress as:

$$(1-n)\rho_s\frac{d^{(s)}\boldsymbol{v}_s}{dt} = \mathrm{div}\,\boldsymbol{\sigma} + n\,\mathrm{grad}\,p_w + (1-n)\rho_s\boldsymbol{b} + (1-n)\boldsymbol{R}_s$$
$$n\rho_w\frac{d^{(w)}\boldsymbol{v}_w}{dt} = \mathrm{div}\,\boldsymbol{\sigma}^{(w)} + p_w\,\mathrm{grad}\,n + n\rho_w\boldsymbol{b} + n\boldsymbol{R}_w \tag{27}$$

and

$$\begin{aligned}(1-n)\rho_s\frac{d^{(s)}\boldsymbol{v}_s}{dt} &= \operatorname{div}\boldsymbol{\sigma}^{(s)} - p_w \operatorname{grad} n + (1-n)\rho_s\boldsymbol{b} + (1-n)\boldsymbol{R}_s \\ n\rho_w\frac{d^{(w)}\boldsymbol{v}_w}{dt} &= \operatorname{div}\boldsymbol{\sigma}^{(w)} + p_w \operatorname{grad} n + n\rho_w\boldsymbol{b} + n\boldsymbol{R}_w\end{aligned} \tag{28}$$

2.3 | Interaction laws

For a Darcy flow, $\boldsymbol{R}$ is given by:

$$\boldsymbol{R} = n^2\boldsymbol{k}_w{}^{-1}(\boldsymbol{v}_w - \boldsymbol{v}_s) = nk_w{}^{-1}\boldsymbol{w} \tag{29}$$

where $\boldsymbol{k}_w$ is the permeability tensor. Its components have dimensions $[k_w] = L^3TM^{-1}$. In case of isotropy, it is given by:

$$\boldsymbol{k}_w = \frac{k^{in\,tr}}{\mu_w}\boldsymbol{I} \tag{30}$$

where $k^{in\,tr}$ is the intrinsic permeability with dimensions L^2 and μ_w is the viscosity of pore fluid. In geotechnical analysis, the permeability is usually defined in a slightly different way as:

$$\overline{k}_w = k_w g\rho_w \tag{31}$$

where g is the acceleration of gravity. In this case, its dimensions are LT^{-1}. Other alternatives[2,9] can be used when the relative velocity is larger:

$$\boldsymbol{R} = \frac{n(1-n)}{V_T n^m}(\rho_s - \rho_w)g(\boldsymbol{v}_w - \boldsymbol{v}_s) \tag{32}$$

where

V_T is the terminal velocity of solid particles falling in the fluid
g the acceleration of gravity
m a constant

Please note that in both cases, we can express the interaction term as

$$\boldsymbol{R} = C_d(\boldsymbol{v}_w - \boldsymbol{v}_s) \tag{33}$$

where C_d is

$$C_d = n^2k_w^{-1} \text{ (Darcy)} \tag{34}$$

or

$$C_d = \frac{n(1-n)}{V_T n^m}(\rho_s - \rho_w)g \text{ (Anderson)} \tag{35}$$

The equations describing the balance of mass and momentum for the mixture are, therefore, the same as those proposed by Pitman and Le in 2005[2] in their 2-fluid model. They have to be complemented by suitable constitutive relations and kinematic equations relating velocities to rate of deformation tensors for both phases.

2.4 | The $\boldsymbol{v_s - v_w - p_w}$ and $\boldsymbol{v_s - p_w}$ Biot-Zienkiewicz models

The general model described by Equations 21, 23, 24, and 25 can be simplified in cases where velocities of both phases are similar by assuming that

$$\frac{d^{(w)}}{dt} \approx \frac{d^{(s)}}{dt} = \frac{d}{dt} \tag{36}$$

which implies that the term $\frac{\boldsymbol{w}^T}{n}.\text{grad}$ is small. Taking 36 into account and adding up the balance of momentum equations 24 and 25, the following balance of momentum for the mixture is obtained

$$\rho\frac{d\boldsymbol{v}}{dt} + n\rho_w\frac{d}{dt}\left(\frac{w}{n}\right) = \text{div}\,\boldsymbol{\sigma}' - \text{grad}\,p_w + \rho\boldsymbol{b} \tag{37}$$

where ρ is the mixture density and $\boldsymbol{v}$ the velocity of the solid skeleton.

Moreover, if porosity is assumed to be constant, the resulting model is written in terms of the unknowns: v_s, v_w, σ', and p_w and consists of the following 4 equations: balance of mass of the mixture 21, balance of momentum of both the mixture 37 and of the fluid phase 25, and a suitable constitutive equation relating the rate of deformation $d_s = \text{grad}_{sym} v_s$ to the rate of effective stress tensors. The resulting model can be casted in terms of v_s, v_w and p_w, hence its name.

In some cases,[24,26] the relative velocity of the pore fluid can be eliminated. The resulting model is the much celebrated $\boldsymbol{u} - p_w$ or $\boldsymbol{v}_s - p_w$ model which is found in most geotechnical finite element codes used today. The equations of the $\boldsymbol{v}_s - p_w$ model are as follows:

(i) Balance of linear momentum equations for the solid and pore fluid can be combined using 36, which results on:

$$\rho\frac{d\boldsymbol{v}}{dt} = \text{div}\,\boldsymbol{\sigma}' - \text{grad}\,p_w + \rho\boldsymbol{b} \tag{38}$$

(ii) From the balance of momentum for the pore fluid, the Darcy's relative velocity w is obtained as described before for the general case:

$$\frac{1}{Q}\frac{dp_w}{dt} + \text{div}\,\boldsymbol{v}_s - \text{div}\,(k_w\,\text{grad}\,p_w) = 0 \tag{39}$$

where we have neglected[1] the term $\text{div}\,(-\rho_w b + \rho_w(dv/dt))$ because body forces will not depend in general on space coordinates (except in centrifuge tests) and the space derivatives of accelerations are assumed to be small.

This model, proposed by Zienkiewicz and Shiomi in 1984[1] for the case of saturated soils, is referred to as $\boldsymbol{u} - p_w$ and consists of Equations 38 and 39, complemented by a constitutive relation for the soil and a kinematic relation linking the velocities to the rate of deformation tensor. The model has been extended to unsaturated soils in Zienkiewicz et al,[27] being worth mention[25] by Lewis and Schrefler.

The original model was developed for solids, which were saturated with water. The authors have applied the model for dry soils, with voids filled with air, to model the flowslide of Las Colinas caused by the first of 2001 earthquakes. Collapse of a metastable soil caused the increase of air pressures, resulting on what it can be called dry liquefaction.[11,28]

2.5 | The two-fluid $v_s - v_w - p_w$ depth averaged model of Pitman and Le

So far, we have considered three 3D continuum models which can describe flow of saturated geomaterials, the most general being that of Equations 16 and 27, complemented by suitable constitutive/rheological and kinematic relations for both phases, which can be applied to debris flows. It is important to notice that these equations describe both triggering and propagation phase.

Debris flows propagate long distances, and the computational cost of a full 3D model can be very high. The problem is similar to those found in coastal hydrodynamics and hydraulics engineering, where depth integrated models have been used since the work of Barré de Saint Venant in 1871,[29] as they provide a reasonable compromise between computational cost and accuracy.

Depth integrated models have been used to study landslide propagation since Savage and Hutter[30] who proposed their much celebrated 1D lagrangian model. Further research by Hutter and Koch,[31] Hutter and co-workers,[32] and Gray

and co-workers[33] extended it to more general conditions. It has been applied by many other researches,[11,12,20-22,34,35] being worth mentioning the textbook by Pudasaini and Hutter.[36] The interested reader will find in Hutter et al[37] an interesting account of the limitations of Savage-Hutter and depth integrated models.

Regarding coupling with the pore fluid, pore pressures change, and so do effective stresses. In consequence, basal friction and mobility of the soil mass will be much affected. Most of the models developed so far assume that velocities of solid skeleton and pore fluid are similar ($\boldsymbol{v}-p_w$ approximation). The first models addressing this issue are those of Hutchinson,[38] who proposed in 1986 a simple sliding-consolidation mechanism for a block, Iverson[39] and Iverson and Denlinger.[10] Wang and Hutter[40] proposed a more general approach, based on mixture theory, in 1999.

We will show here how $\boldsymbol{v}-p_w$ depth integrated models can be considered as a particular case of the 2-fluid $\boldsymbol{v}_s-\boldsymbol{v}_w-p_w$ depth averaged models.

We will use the reference system with axes $\{x_1, x_2, x_3\}$ sketched in Figure 1. Z will denote the basal surface elevation, and h the depth of the flowing mass. Velocities will be denoted as $\{v_1, v_2, v_3\}$, and sub indexes s and w will refer to solid and fluid phases.

An over bar over a magnitude indicates it is a depth averaged value. For instance:

$$\overline{\theta} = \frac{1}{h}\int_Z^{Z+h} \theta \, dx_3$$

We will define the mixture averaged velocity $\overline{v}$

$$\overline{\boldsymbol{v}} = (1-\overline{n})\overline{\boldsymbol{v}}_s + \overline{n}\,\overline{\boldsymbol{v}}_w \tag{40}$$

and the "quasi material derivative" as:

$$\frac{\overline{d}}{dt} = \frac{\partial}{\partial t} + \overline{v}_j \frac{\partial}{\partial x_j} \quad j = 1, 2 \tag{41}$$

Depth integration is performed taking into account Leibnitz's rule

$$\int_a^b \frac{\partial}{\partial s} F(r,s)\, dr = \frac{\partial}{\partial s}\int_a^b F(r,s)\, dr - F(b,s)\frac{\partial b}{\partial s} + F(a,s)\frac{\partial a}{\partial s} \tag{42}$$

After integrating along depth and applying 42 to the **balance of mass equations** 16, the following depth integrated expressions are obtained:

$$\begin{aligned} &\frac{\overline{d}^{(s)}}{dt}((1-\overline{n})h) + (1-\overline{n})h \ \mathrm{div}\,\overline{\boldsymbol{v}}_s = (1-\overline{n})\, e_R \\ &\frac{\overline{d}^{(w)}}{dt}(\overline{n}\,h) + \overline{n}\,h \ \mathrm{div}\,\overline{\boldsymbol{v}}_w = \overline{n}\, e_R \end{aligned} \tag{43}$$

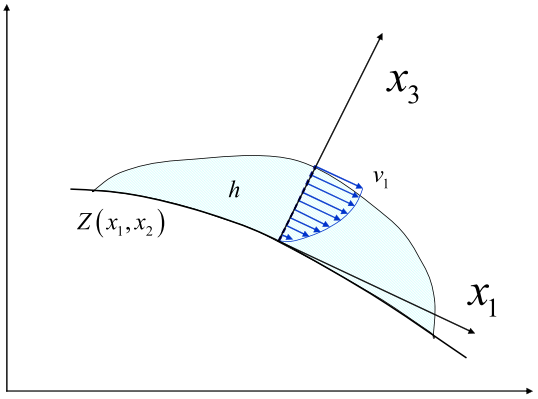

FIGURE 1 Reference system, coordinates, and notation used in the analysis [Colour figure can be viewed at wileyonlinelibrary.com]

where e_R is the erosion rate, defined as the increment of height of the moving soil per unit time. There are laws such as that proposed by Hungr and coworkers[41] in 2005, which relates it to the depth averaged velocity of the flowing material. Both equations in 43 can be rewritten as:

$$\begin{aligned} &\frac{\overline{d}^{(\alpha)}}{dt}(\overline{n}_\alpha h) + \overline{n}_\alpha h \ \mathrm{div}\,\overline{\boldsymbol{v}}_\alpha = \overline{n}_\alpha e_R \ \text{ or} \\ &\frac{\overline{d}^{(\alpha)}}{dt}(h_\alpha) + h_\alpha \ \mathrm{div}\,\overline{\boldsymbol{v}}_\alpha = \overline{n}_\alpha e_R \end{aligned} \tag{44}$$

where

$$\begin{aligned} &\alpha = \{s, w\} \quad h_\alpha = \overline{n}_\alpha h \\ &\overline{n}_s = (1-\overline{n}) \quad \overline{n}_w = \overline{n} \end{aligned} \tag{45}$$

Above equations—without the erosion rates—have been proposed by Pitman and Le in their 2-fluid model.[2] If velocities of solid and fluid particles are assumed to be similar, then 44 reads:

$$\frac{\overline{d}h}{dt} + h \ \mathrm{div}\,\overline{\boldsymbol{v}} = e_R \tag{46}$$

where

$$\frac{\overline{d}h}{dt} \approx \frac{\overline{d}^{(s)}h}{dt} \approx \frac{\overline{d}^{(w)}h}{dt}$$

Regarding the **balance of momentum equations** 24 and 25 for both phases, after integrating along depth (local x_3 axis), we arrive to:

$$\begin{aligned} \rho_s h(1-\overline{n})\frac{\overline{d}^{(s)}\overline{\boldsymbol{v}}_s}{dt} &= \mathrm{div}(h\overline{\boldsymbol{\sigma}}') - (1-n)\ \mathrm{grad}\,(h\overline{p}_w) + \boldsymbol{\tau}_{b^{(s)}} + (1-\overline{n})h\overline{\boldsymbol{R}}_s + (1-\overline{n})\rho_s \boldsymbol{b}h - (1-\overline{n})\rho_s \overline{\boldsymbol{v}}_s e_R \\ \rho_w h\,\overline{n}\frac{\overline{d}^{(w)}\overline{\boldsymbol{v}}_w}{dt} &= -n\ \mathrm{grad}\,(h\overline{p}_w) + \boldsymbol{\tau}_{b^{(w)}} + \ \overline{n}h\overline{\boldsymbol{R}}_w + \overline{n}\rho_w \boldsymbol{b}h - \overline{n}\rho_w \overline{\boldsymbol{v}}_w e_R \end{aligned} \tag{47}$$

where we have introduced the shear basal stresses of the solid and fluid phases as:

$$\boldsymbol{\tau}_{b\,i^{(s)}} = \ -\sigma_{i\,3^{(s)}}\big|_Z \quad \boldsymbol{\tau}_{b\,i^{(w)}} = \ -\sigma_{i\,3^{(w)}}\big|_Z \tag{48}$$

In terms of the partial stress tensor, the balance of momentum for the solid phase is

$$\rho_s h(1-\overline{n})\frac{\overline{d}^{(s)}\overline{\boldsymbol{v}}_s}{dt} = \mathrm{div}\left(h\overline{\boldsymbol{\sigma}}^{(s)}\right) - h\overline{p}_w\,\mathrm{grad}\,(n) + \boldsymbol{\tau}_{b^{(s)}} + (1-\overline{n})h\overline{\boldsymbol{R}}_s + (1-\overline{n})\rho_s \boldsymbol{b}h - (1-\overline{n})\rho_s \overline{\boldsymbol{v}}_s e_R \tag{49}$$

and, in terms of the total stress tensor 49 reads

$$\rho_s h(1-\overline{n})\frac{\overline{d}^{(s)}\overline{\boldsymbol{v}}_s}{dt} = \mathrm{div}(h\overline{\boldsymbol{\sigma}}) + \overline{n}\ \mathrm{grad}(h\overline{p}_w) + \boldsymbol{\tau}_{b^{(s)}} + (1-\overline{n})h\overline{\boldsymbol{R}}_s + (1-\overline{n})\rho_s \boldsymbol{b}h - (1-\overline{n})\rho_s \overline{\boldsymbol{v}}_s e_R \tag{50}$$

One special case of interest is when stresses in the solid phase can be considered as hydrostatic and the pore fluid is inviscid. If the pore fluid pressure is considered to be composed of an hydrostatic and an excess components, the latter component denoted as Δp_w, then the normal components of the total stress and the fluid partial stress $\boldsymbol{\sigma}^{(w)}$ can be written as:

$$\begin{aligned} &\sigma_{ii} = ((1-n)\rho_s + n\rho_w)b_3(h-x_3), \quad i = 1,2,3 \\ &\sigma_{ii^{(w)}} = n\rho_w b_3(h-x_3) - n\,\Delta p_w, \quad i = 1,2,3 \end{aligned} \tag{51}$$

using 11 and 13, the normal components of the effective stress and the solid partial stress $\boldsymbol{\sigma}^{(s)}$ can be written as:

$$\begin{aligned}\sigma_{ii^{(s)}} &= (1-n)\rho_s b_3(h-x_3) + n\Delta p_w, \quad i=1,2,3\\ \sigma'_{ii} &= (1-n)(\rho_s-\rho_w)b_3(h-x_3) + \Delta p_w, \quad i=1,2,3\end{aligned} \tag{52}$$

After substituting in 49 the expression for the solid partial stress $\boldsymbol{\sigma}^{(s)}$ that appears in 52, the depth integrated equation for the solid phase reads:

$$\rho_s h(1-\overline{n})\frac{\overline{d}^{(s)}\overline{\boldsymbol{v}}_s}{dt} = \operatorname{grad}\left\{\frac{1}{2}(1-\overline{n})\rho_s h^2 b_3\right\} + \frac{1}{2}\rho_w h^2 b_3 \operatorname{grad}\overline{n} + \boldsymbol{\tau}_{b^{(s)}} + (1-\overline{n})h\overline{\boldsymbol{R}}_s + (1-\overline{n})\rho_s \boldsymbol{b}h - (1-\overline{n})\rho_s \overline{\boldsymbol{v}}_s e_R \tag{53}$$

Similarly, after substituting the expression for the fluid partial stress $\boldsymbol{\sigma}^{(w)}$ that appears in 51 the depth integrated balance of momentum of the fluid phase 47 reads

$$\rho_w h\overline{n}\frac{d^{(w)}\boldsymbol{v}_w}{dt} = \operatorname{grad}\left\{\frac{1}{2}\overline{n}\rho_w h^2 b_3\right\} - \frac{1}{2}\rho_w h^2 b_3 \operatorname{grad}\overline{n} + \boldsymbol{\tau}_{b^{(w)}} + \overline{n}h\overline{\boldsymbol{R}}_w + \overline{n}\rho_w \boldsymbol{b}h - \overline{n}\rho_w \overline{\boldsymbol{v}}_w e_R \tag{54}$$

As per expressions 53 and 54, it is clear that we have not considered the excess pore pressures, following Pitman and Le.[2] By excess pore pressures, we consider those in excess of the hydrostatic pressure, which is equivalent to assume that permeability is very large. This is a limitation of the proposed model.

Balance of mass and momentum for both phases can be written in a more compact form as:

$$\frac{\overline{d}^{(\alpha)}}{dt}(h_\alpha) + h_\alpha \operatorname{div}\overline{\boldsymbol{v}}_\alpha = \overline{n}_\alpha e_R \tag{55}$$

and

$$\rho_\alpha h_\alpha \frac{d^{(\alpha)}\overline{\boldsymbol{v}}_\alpha}{dt} = \operatorname{grad}\left\{\frac{1}{2}\rho_\alpha h h_a b_3\right\} - \frac{1}{2}\rho_\alpha h^2 b_3 \operatorname{grad}\overline{n}_\alpha + \boldsymbol{\tau}_{b^{(\alpha)}} + h_\alpha \overline{\boldsymbol{R}}_\alpha + \rho^\alpha h_\alpha \boldsymbol{b} - \overline{n}_\alpha \rho_\alpha \overline{\boldsymbol{v}}_\alpha e_R \tag{56}$$

where α denotes the phase (s or w), $\overline{n}_\alpha$ being the volume fractions of solid and fluid phases ($n_s = 1-n$ and $n_w = n$), and $h_\alpha = h\overline{n}_a$.

For convenience, from now on, we will drop the over bar, all magnitudes being depth integrated unless otherwise stated.

Hydrostatic distribution stress components for the solid have been assumed, the more general case of active-passive Mohr-Coulomb stresses proposed by Hutter[32] being described in Pitman and Le[2] Regarding the fluid, during depth integration, we have assumed a hydrostatic state as done for solids.

Equations 55 and 56 describe the evolution of height h, porosity n, and velocities of solid and fluid. The pore pressure can be obtained from the balance of momentum equation for the fluid.

2.6 | Biot-Zienkiewicz $v_s - p_w$ depth averaged model

The aim of this section is to relate the general model described above to those used in the past by Swansea group, which were derived from the general model. These 3D models have been extensively used in geotechnical codes. Here, we use a depth integrated model derived from the more general 3D model, which is a generalization of previous works done by the authors with the $\boldsymbol{v} - p_w$ model.[12,15]

The general 2-fluid depth integrated equations described above can be simplified if we assume, like in the $\boldsymbol{v}_s - p_w$ model, that $\frac{d^{(w)}}{dt} \approx \frac{d^{(s)}}{dt} = \frac{d}{dt}$ and neglect the acceleration of the fluid relative to the solid. Equation 44 results on:

$$\frac{\overline{d}h}{dt} + h \operatorname{div}\boldsymbol{v} = e_R \tag{57}$$

While the balance of linear momentum equations yield, in a similar manner:

$$\rho h \frac{\overline{d}\boldsymbol{v}}{dt} = \frac{1}{2}\,\mathrm{grad}\left(\rho h^2 b_3\right) + \boldsymbol{\tau}_b + \rho h\,\boldsymbol{b} - \rho \boldsymbol{v} e_R \tag{58}$$

The basal shear stress depends on the rheological law used. In the case of a pure frictional material, it is given by $-\{(\rho_s - \rho_w)(1-n)hb_3 + \Delta p_{wb}\}\frac{\boldsymbol{v}_s}{\|\boldsymbol{v}_s\|}\tan\phi_b$ where ϕ_b is the friction angle and Δp_{wb} the increment of pore water pressure at the basal surface.

It is important to note that the effect of centripetal accelerations needs to be included. This can be done in a simple manner by integrating along the vertical the balance of momentum equation assuming a constant vertical acceleration given by $\overline{v}^2/R$, where $\overline{v}$ is the modulus of the averaged velocity and R the main radius of curvature in the direction of the flow.

3 | A SPH MODEL FOR THE TWO-PHASE DEPTH AVERAGED MODEL OF PITMAN AND LE

3.1 | Introduction

Problems in solid and fluid mechanics involve large deformations in many occasions. In the case of fluids, classical finite element and FD techniques have been widely used in the past, using eulerian formulations. On the other hand, solids have been studied using lagrangian finite element formulations. In both cases, special techniques have been necessary to obtain the free surface or largely distorted meshes.

The situation has improved with the development of a new class of numerical methods that are not based on meshes mdash;even if they can be used as an auxiliary tool—but on points or nodes, where functions and derivatives are approximated. Among these methods, we can mention the diffuse element method,[42] the element free Galerkin,[43] the hp-cloud method,[44] the partition of unity method,[45] the finite point method,[46,47] MPM,[48-52] and, finally, the SPH method, which is the technique which will be described here.

SPH was introduced independently by Lucy[53] and Gingold and Monaghan[54] in 1977 for astronomical modeling. Since then, it has been applied to model problems in hydrodynamics[55], flow trough porous media,[56] shallow water flows,[57-61] and avalanche propagation,[12,22,23] just to mention a few representative cases. Good reviews can be found in the textbooks like.[62,63]

SPH presents here the advantage of a much simpler determination of free surfaces and interfaces, avoiding special techniques such as the Level Set.

In the case of solids, the main advantage is its lagrangian nature. Nodes carry information regarding all constitutive information required by advanced models, while eulerian methods have to convect this information, loosing consistency. For instance, the condition of the stress belonging to a yield surface depends both on the stress tensor and the history parameters, which are convected separately. It is worth mentioning the contributions of Libersky and co-workers,[64,65] Randles and Libersky,[66,67] Bonet and Kulasegaram,[68] and Gray and co-workers.[69]

Soils are a special case of solids where the solid skeleton is filled with pore fluids, which interact with it. SPH has been applied to model coupling and failure problems of soils recently.[17,70-72]

Landslides, avalanches, and other similar phenomena can propagate long distances. In order to assess the risk and propose measures, it is necessary to predict their velocity, height, and run out. 3D modeling of fast propagating landslides requires in most cases a large computational effort. An interesting alternative combining a good accuracy with a more affordable cost is using depth integrated models.

SPH based depth averaged models for landslide propagation have been used in Pastor et al,[12] McDougall and Hungr,[22] and Rodriguez-Paz and Bonet.[23] An improved method for pore pressure dissipation, based on combining the SPH nodes with FD 1D meshes associated to them, has been recently proposed by Pastor and co-workers.[15]

The mathematical model proposed is basically the one proposed in 2005 by Pitman and Le,[2] the originality being its formulation using a SPH model. However, it is also truth that our equations include terms describing erosion, and these terms were not considered in Pitman and Le 2005 formulation.

Here, we propose a new approach based on a double set of nodes to model debris flows. One set for the solid particles and the other for the pore fluid.

3.2 | SPH: Fundamentals and special problems

The SPH method is based on approximating functions and differential operators such as gradient or divergence by integral approximations defined in terms of a kernel. In a second step, these integral representations are approximated numerically by a class of numerical integration based on a set of discrete point or nodes, without having to define any "element".

The approximation of a given function $\phi(x)$ is written as

$$\langle \phi(x) \rangle = \int_{\Omega} \phi(x') W(x'-x, h) dx' \tag{59}$$

where $W(x'-x, h)$ is referred to as the kernel of the linear functional, h being a parameter describing its decay. A special class of kernels is that of functions having radial symmetry, ie, depending only on r:

$$r = |x'-x| \tag{60}$$

It is convenient to introduce the notation:

$$\xi = \frac{|x'-x|}{h} = \frac{r}{h} \tag{61}$$

The functions *W(x,h)* used as kernels in SPH approximations are required to fulfill the following conditions:

(i)

$$\lim_{h \to 0} W(x'-x, h) = \delta(x) \tag{62}$$

(ii)

$$\int_{\Omega} W(x'-x, h) dx' = 1 \tag{63}$$

Condition 63, which also follows from 62, can be interpreted as well as the ability of the approximation to reproduce a constant or polynomial of degree zero (zero order consistency).

(iii) The kernel $W(x'-x, h)$ is positive and has compact support

$$W(x'-x, h) = 0 \quad if \quad |x'-x| \geq kh \tag{64}$$

where k is a positive integer which is usually taken as 2.

(iv) The kernel $W(x'-x, h)$ is a monotonically decreasing function of ξ.

(v) The kernel is an even function with respect to ξ.

It is possible to show that, under the conditions specified above, the approximation is second order accurate, ie,

$$\langle \phi(x) \rangle = \phi(x) + O(h^2) \tag{65}$$

It is interesting to note that the integral approximation 59 is nothing but a linear functional, which is usually denoted as

$$T_h[\phi] = \int_{\Omega} W(x', h) \phi(x') dx' \tag{66}$$

Moreover, it can be seen that the limit of $T_h[\phi]$ as h tends towards zero

$$\lim_{h \to 0} T_h[\phi] = \delta[\phi] \tag{67}$$

is the Dirac delta, which is a singular transformation. It is possible to write:

$$\phi(x) = \int_{\Omega}\phi(x')\,\delta(x'-x)dx' \tag{68}$$

In the framework of SPH formulations, several kernels have been proposed in the past. Among them, it is worth mentioning: (1) the Gaussian kernel[54] and (2) the cubic spline.[73,74] Concerning the integral representation of the derivatives in SPH, we have:

$$\langle\phi'(x)\rangle = \int_{\Omega}\phi'(x')W(x'-x,h)dx' \tag{69}$$

After integration by parts—in a 1-dimensional problem—and taking into account that the kernel has compact support, 69 reads:

$$\langle\phi'(x)\rangle = -\int_{\Omega}\phi(x')W'(x'-x,h)dx' \tag{70}$$

Classical differential operators of continuum mechanics can be approximated in the same way. We list below the gradient of a scalar function, the divergence of a vector function, and the divergence of a tensor function:

$$\langle\,\mathrm{grad}\phi(x)\rangle = -\int_{\Omega}\phi(x')\frac{1}{h}W'\,\frac{x'-x}{r}d\Omega \;\text{ with }\; r = |x'-x| \tag{71}$$

$$\langle\,\mathrm{div}\,\boldsymbol{u}(x)\rangle = -\int_{\Omega}\boldsymbol{u}(x')\,\mathrm{grad}\,Wd\Omega = -\int_{\Omega}\frac{1}{h}W'\,\frac{\boldsymbol{u}(x').(x'-x)}{r}d\Omega \tag{72}$$

$$\langle\,\mathrm{div}\,\boldsymbol{\sigma}(x)\rangle = -\int_{\Omega}\boldsymbol{\sigma}.\,\mathrm{grad}\,Wd\Omega = -\int_{\Omega}\frac{1}{h}W'\,\frac{\boldsymbol{\sigma}.(x'-x)}{r}d\Omega \tag{73}$$

These approximations of functions and derivatives are valid at continuum level. If the information is stored in a discrete manner, for instance, in a series of points or nodes, it is necessary to construct discrete approximations. The SPH method introduces the concept of "particles", to which information concerning field variables and their derivatives is linked. But indeed, they are nodes, much in the same way than found in finite elements or FDs. All operations are to be referred to nodes. We will therefore introduce the set of particles or nodes with $K = 1...N$. Of course, the level of approximation will depend on how the nodes are spaced and on their location. The classical finite element strategy of having more nodes in those zones where larger gradients are expected is of application here.

As per the last paragraph, evaluation of an integral approximation like 59 can be performed using a numerical integration technique of the type:

$$\langle\phi(x_I)\rangle_h = \sum_{J=1}^{N}\phi(x_J)W(x_J-x_I,h)\,\omega_J \tag{74}$$

where the information of the given function $\phi(x)$ is only available at a set of N nodes within the domain Ω. In 74, the sub index "h" has been used to denote the discrete approximation, with ω_J denoting the weights of the integration formula—which can be shown to be $\omega_J = \Omega_J = m_J/\rho_J$, with Ω_J, m_J and ρ_J being the volume, mass, and densities associated to node J. In order to simplify the representation, the following notation is introduced:

$$\phi_I = \langle\phi(x_I)\rangle_h = \sum_{J=1}^{N}\phi(x_J)W(x_J-x_I,h)\,\Omega_J \tag{75}$$

Taking into account 64, that is to say, the kernel function has local support, then expression 75 reads

$$\phi_I = \langle \phi(x_I) \rangle_h = \sum_{J=1}^{Nh} \phi(x_J) W(x_J - x_I, h)\, \Omega_J \tag{76}$$

Where x_J with $J = 1 \ldots Nh$ is the set of nodes fulfilling the relation $|x_J - x_I| < kh$. In the case the function ϕ represents the density, 76 becomes

$$\begin{aligned} \rho_I &= \sum_{J=1}^{Nh} \rho_J W_{IJ} \frac{m_J}{\rho_J} \\ \rho_I &= \sum_{J=1}^{n} W_{IJ}\, m_J \end{aligned} \tag{77}$$

with $W_{IJ} = W(x_J - x_I, h)$.

One interesting aspect of SPH is the existence of several alternative discretized forms for the differential operators. For instance, the gradient of a scalar function can be approximated as (basic form):

$$\mathrm{grad}\phi_I = \sum_{J=1}^{Nh} \frac{m_J}{\rho_J} \phi_J\, \mathrm{grad}\, W_{IJ} \tag{78}$$

and also by the following symmetrized forms

$$\mathrm{grad}\phi_I = \frac{1}{\rho_I} \sum_J m_J (\phi_J - \phi_I)\, \mathrm{grad} W_{IJ} \tag{79}$$

$$\mathrm{grad}\phi_I = \rho_I \sum_J m_J \left\{ \frac{\phi_J}{\rho_J^2} + \frac{\phi_I}{\rho_I^2} \right\} \mathrm{grad} W_{IJ} \tag{80}$$

Sometimes, it is preferred to use a variant of this form, which is

$$\mathrm{grad}\phi_I = \sum_{J=1}^{Nh} \frac{m_J}{\rho_J} (\phi_I + \phi_J)\, \mathrm{grad} W_{IJ} \tag{81}$$

3.3 | Special problems

As any numerical method, SPH presents some problems which have to be taken into account as they can result on unphysical oscillations and loss of accuracy.

(i) *Boundary deficiency*

Close to boundaries, the integration is carried out only over points belonging to the domain, and not over the whole support of the kernel. If we have a body with constant density and we try to compute it at the boundaries, we obtain smaller values. The problem was detected by Morris in 1985,[75] and since then, several remedial techniques have been proposed.[62,67,76] We have applied normalization to nodes close to boundaries of wall type.

(ii) *Stability*

SPH presents, in materials with strength, the tensile instability problem, which consists of unphysical clumping of particles from where the instability may grow.[68] Swegle and co-workers[77] in 1995 described the problem in 2-dimensional arrangements of particles and studied the stability, which was found to depend on the properties of the kernel. To remediate the problem, several alternative methods have been proposed:

(i) Use of special kernel functions.[75]

(ii) Introducing artificial stabilizing forces.[69,78] Generally, this force is called artificial stress and consists on repulsion when neighboring particles get closer

(iii) Adding a new set of stress points between the SPH nodes. The stress is calculated on the stress points using the information of the SPH nodes, and the linear momentum is calculated on the SPH nodes from the stress points. This method has been first proposed by Dyka for 1-dimensional problems with the following SPH nodes arrangement: 2 stress points for 1 SPH node.[79,80] This method has been extended to 2-dimensional problems by Randles and Libersky.[66,67]

(iv) Blanc and Pastor have proposed recently[17,18] a novel SPH algorithm which is an extension of the Taylor Galerkin method proposed in Peraire et al[81] and Donea et al[82] and subsequently extended[83] to solid dynamics problems. It uses a double set of SPH nodes.

(v) *Boundary conditions*

Boundary conditions require special treatment in SPH. In addition to the boundary deficiency problem and the solutions already mentioned, SPH practitioners use special virtual particles located at the boundaries. Monaghan introduced[84] in 1982 a first type of virtual particles, often referred to as "type 1 virtual particles", which apply a repulsive force on particles approaching the boundary, which prevents boundary penetration by them.

Libersky and co-workers[65] in 1993, and Randles and Libersky[66] in 1996 introduced a second type of virtual particles, which are located symmetrically respect to the real particle approaching the boundary.

These methods have been improved by Bonet and co-workers[85] in 2004 for cases where rigid boundaries are present.

In the case of shallow water waves, boundary conditions of absorbing and prescribed incoming waves are important and have been studied by several researches.[86,87]

When dealing with solid walls, such as those impounding fluidized soils in dam break examples shown below, we have applied a simple boundary condition which detects those nodes close to the wall, and filtering the velocity component along the normal to the wall.

3.4 | Proposed SPH model

Following the procedure outlined in previous sections, we will introduce:

(i) 2 sets of nodes $\{x_{\alpha K}\}$ with $K=1\ldots N_\alpha$ where N_s and N_w are the number of SPH nodes in the solid and fluid phases,

(ii) The nodal variables

$h_{\alpha I}$ heights of phases at node I

$\overline{\boldsymbol{v}}_{\alpha I}$ depth averaged, 2D velocities

$\boldsymbol{\tau}_{bI^{(\alpha)}}$ shear stress at the bottom

We will recall here for convenience the balance of mass and momentum equations 55 and 56:

$$\frac{\overline{d}^{(\alpha)}}{dt}(h_\alpha)+h_\alpha\,\mathrm{div}\,\overline{\boldsymbol{v}}_\alpha=\overline{n}_\alpha e_R$$

and

$$\rho_\alpha h_\alpha\frac{d^{(\alpha)}\overline{\boldsymbol{v}}_\alpha}{dt}=\mathrm{grad}\left\{\frac{1}{2}\rho_\alpha h h_a b_3\right\}-\frac{1}{2}\rho_\alpha h^2 b_3\,\mathrm{grad}\,\overline{n}_\alpha+\boldsymbol{\tau}_{b^{(\alpha)}}+h_\alpha\overline{\boldsymbol{R}}_\alpha+\rho^\alpha h_\alpha\boldsymbol{b}-\overline{n}_\alpha\rho_\alpha\overline{\boldsymbol{v}}_\alpha e_R$$

If the 2D area associated to a general fluid or solid node I is Ω_I, we will introduce for convenience, a fictitious volume m_I with dimensions L^3 moving with this node:

$$m_I=\Omega_I h_I \tag{82}$$

It is important to note that m_I has no physical meaning, as when node I moves, the material contained in a column of base Ω_I has entered it or will leave it as the column moves with an averaged velocity which is not the same for all particles in it.

The SPH approximation of the balance of mass equation for both phases is built from

$$\left\langle \frac{\overline{d}h_\alpha}{dt} + h_\alpha \ \mathrm{div}\,\overline{\boldsymbol{v}}_\alpha \right\rangle = \langle \overline{n}_\alpha e_R \rangle \tag{83}$$

from which:

$$\frac{\overline{d}}{dt}\langle h_\alpha \rangle + \langle h_\alpha \rangle \langle \mathrm{div}\,\overline{\boldsymbol{v}}_\alpha \rangle = \langle \overline{n}_\alpha e_R \rangle \tag{84}$$

From now on, when possible, we will drop the sub-indexes for the sake of simplicity. The equation is written at node I as:

$$\frac{\overline{d}}{dt}h_I + h_I \langle \mathrm{div}\,\overline{\boldsymbol{v}} \rangle_I = \langle \overline{n}\, e_R \rangle_I \tag{85}$$

where the divergence term is approximated as:

$$\mathrm{div}\,\overline{\boldsymbol{v}}_I = -\sum_J \Omega_J v_J \ \mathrm{grad}\, W_{IJ} \tag{86}$$

or

$$\mathrm{div}\, v_I = -\sum_J \frac{m_J}{h_J} v_J \ \mathrm{grad}\, W_{IJ} \tag{87}$$

Of course, we could have used any alternative symmetrized form.

The discretized balance of mass equation is written as

$$\begin{aligned}
\frac{\overline{d}h_I}{dt} &= -h_I \sum_J \frac{m_J}{h_J} v_J \ \mathrm{grad}\, W_{IJ} + \langle \overline{n}\, e_R \rangle_I \qquad \text{(Basic form)} \\
\frac{\overline{d}h_I}{dt} &= \sum_J m_J v_{IJ} \ \mathrm{grad}\, W_{IJ} + \langle \overline{n}\, e_R \rangle_I \qquad \text{(1st form)} \\
\frac{\overline{d}h_I}{dt} &= h_I \sum_J \frac{m_J}{h_J} v_{IJ} \ \mathrm{grad}\, W_{IJ} \ + \langle \overline{n}\, e_R \rangle_I \qquad \text{(3rd form)}
\end{aligned} \tag{88}$$

where we have introduced v_{IJ}

$$v_{IJ} = v_I - v_J$$

Alternatively, the height can be obtained once the position of the nodes is known as:

$$\begin{aligned}
h_I &= \langle h(x_I) \rangle \\
&= \sum_J h_J \Omega_J W_{IJ} \\
&= \sum_J m_J W_{IJ}
\end{aligned} \tag{89}$$

The height can be normalized, which allows improving the approximation close to the boundary nodes:

$$h_I = \frac{\sum_J m_J W_{IJ}}{\sum_J \left(\frac{m_J}{h_J} \right) W_{IJ}} \tag{90}$$

Next, we will discretize the balance of linear momentum equation

$$\rho_\alpha h_\alpha \frac{d^{(\alpha)}\overline{\boldsymbol{v}}_\alpha}{dt} = -\rho_\alpha \operatorname{grad}\{P_\alpha\} - \frac{1}{2}\rho_\alpha h^2 b_3 \operatorname{grad}\overline{n}_\alpha + \boldsymbol{\tau}_{b^{(\alpha)}} + h_\alpha \overline{\boldsymbol{R}}_\alpha + \rho^\alpha h_\alpha \boldsymbol{b} - \overline{n}_\alpha \rho_\alpha \overline{\boldsymbol{v}}_\alpha e_R \tag{91}$$

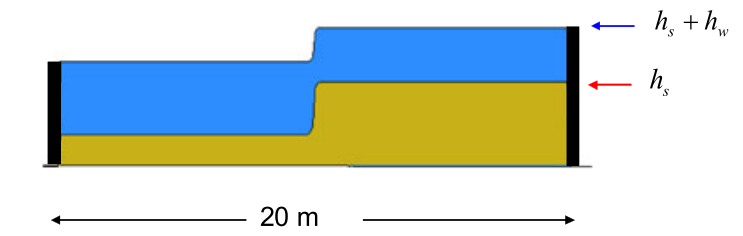

$\rho_s = 2000\,Kg/m^3$

$\rho_w = 1000\,Kg/m^3$

$n_L = 0.69$

$n_R = 0.39$

$\tan\phi = 0.0$

Interaction law (Anderson)

$R = -nR_w = (1-n)R_s$

$R = C_d\left(v_w - v_s\right)$

$C_d = \dfrac{n(1-n)}{V_T n^m}(\rho_s - \rho_w)g$

$V_T = 1.0e-3$

$m = 1$

FIGURE 2 Two-phase dam break problem [Colour figure can be viewed at wileyonlinelibrary.com]

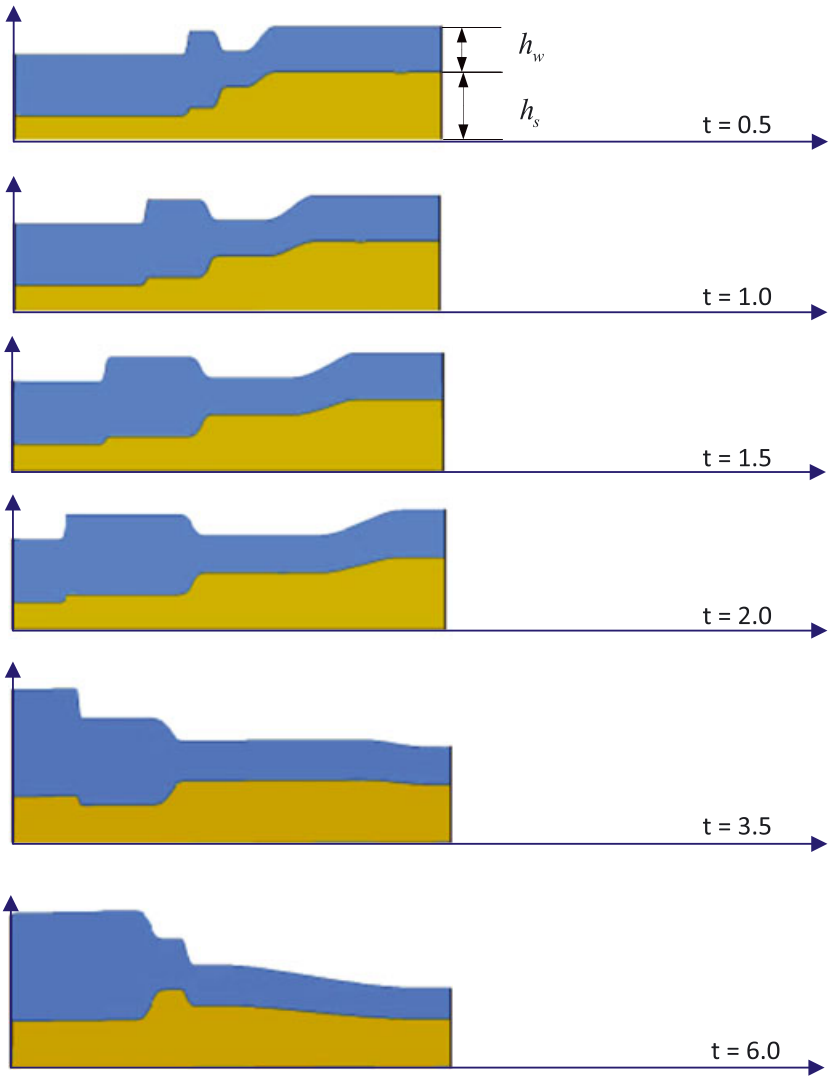

FIGURE 3 Profiles of h_s and $h_s + h_w$ at times 0.5, 1.0, 1.5, 2.0, 3.5, and 6 seconds [Colour figure can be viewed at wileyonlinelibrary.com]

where we have introduced the averaged pressure $P_\alpha = -\frac{1}{2} h h_a b_3$. The left-hand side of 91 results on:

$$\rho_I h_I \frac{\overline{d}}{dt} \overline{v}_I \tag{92}$$

Depending on the symmetrized form chosen[84,88,89] to discretize the gradients of the pressure and the volume fractions, we obtain the following discretized forms of the balance of momentum equation:

$$\frac{\overline{d}^{(\alpha)}}{dt} \overline{v}_{\alpha I} = \sum_J m_J \frac{P_{\alpha I} + P_{\alpha J}}{h_{\alpha I} h_{\alpha J}} \operatorname{grad} W_{IJ} + \sum_J m_J h_J^2 b_3 \frac{n_{\alpha I} + n_{\alpha J}}{h_{\alpha I} h_{\alpha J}} \operatorname{grad} W_{IJ} + \frac{1}{\rho_\alpha h_{\alpha I}} \boldsymbol{\tau}_{b\,I^{(\alpha)}} + \frac{1}{\rho_\alpha} \overline{\boldsymbol{R}}_\alpha + \boldsymbol{b} - \frac{1}{h_{\alpha I}} \overline{n}_\alpha \overline{\boldsymbol{v}}_\alpha e_R \tag{93}$$

$$\frac{\overline{d}^{(\alpha)}}{dt} \overline{v}_{\alpha I} = \sum_J m_J \left(\frac{P_{\alpha I}}{h_I^2} + \frac{P_{\alpha J}}{h_J^2} \right) \operatorname{grad} W_{IJ} + \sum_J m_J h_J^2 b_3 \left(\frac{n_{\alpha I}}{h_I^2} + \frac{n_{\alpha J}}{h_J^2} \right) \operatorname{grad} W_{IJ} + \frac{1}{\rho_\alpha h_{\alpha I}} \boldsymbol{\tau}_{b\,I^{(\alpha)}} + \frac{1}{\rho_\alpha} \overline{\boldsymbol{R}}_\alpha + \boldsymbol{b} - \frac{1}{h_{\alpha I}} \overline{n}_\alpha \overline{\boldsymbol{v}}_\alpha e_R \tag{94}$$

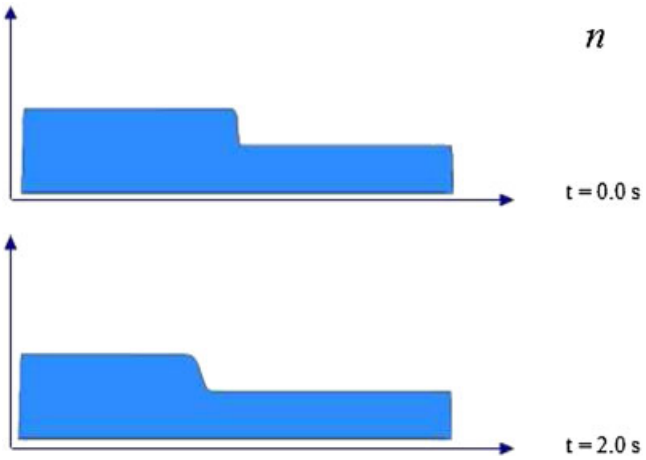

FIGURE 4 Profiles of porosity at times 0 and 2 seconds (values at right and left ends are 0.39 and 0.69, respectively) [Colour figure can be viewed at wileyonlinelibrary.com]

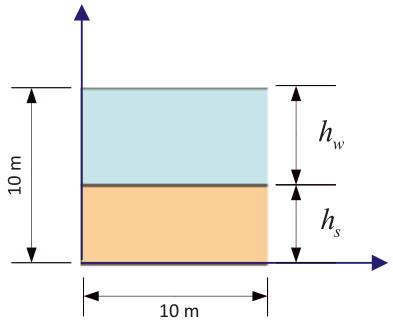

$\rho_s = 2000\ Kg/m^3$ *Interaction law (Anderson)*

$\rho_w = 1000\ Kg/m^3$ $R = -nR_w = (1-n)R_s$

$n_L = 0.69$ $R = C_d(v_w - v_s)$ $V_T = 1.0e-3$

$n_R = 0.39$ $C_d = \frac{n(1-n)}{V_T n^m}(\rho_s - \rho_w)g$ $m = 1$

$\tan\phi = 0.0$

FIGURE 5 Two-phase dam break problem over a horizontal plane ($h_s = 4m$ $h_w = 6m$ $h = 10m$) [Colour figure can be viewed at wileyonlinelibrary.com]

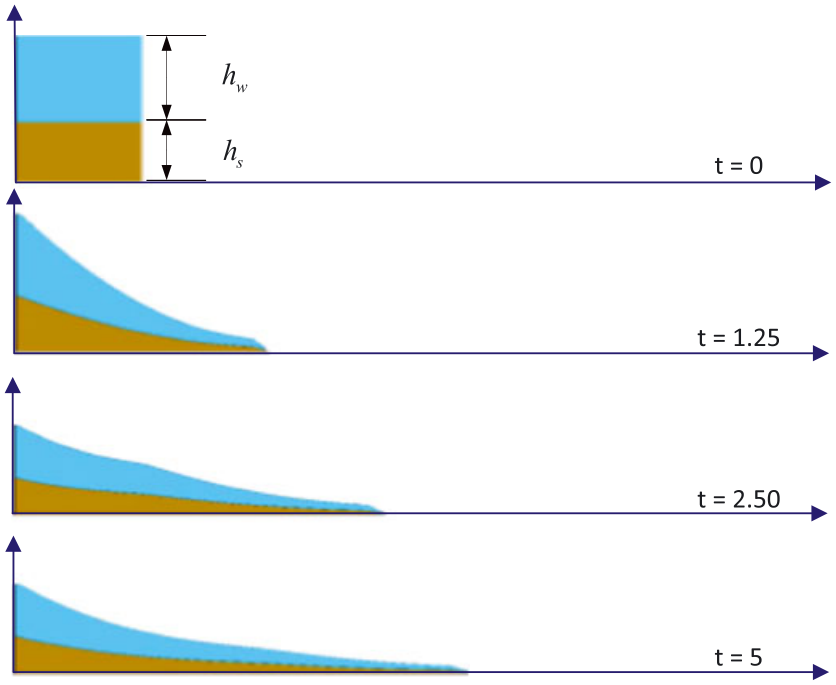

FIGURE 6 Profiles of h_s and $h_s + h_w$ at times 0, 1.25, 2.5, and 5 seconds [Colour figure can be viewed at wileyonlinelibrary.com]

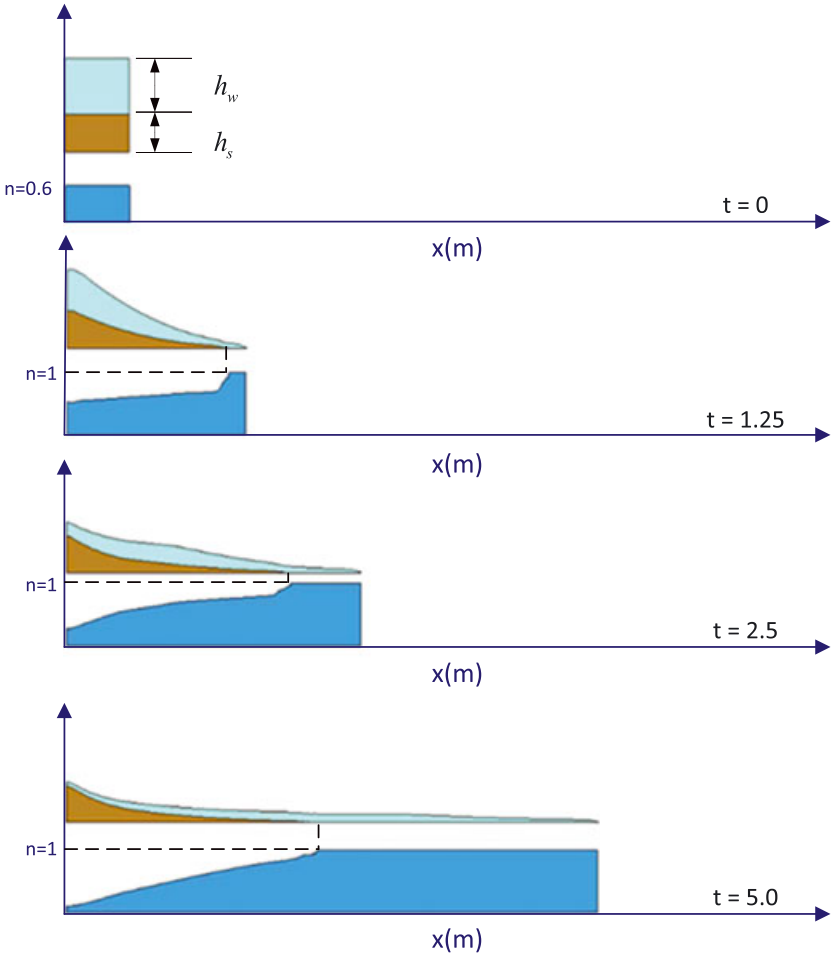

FIGURE 7 Profiles of h_s, $h_s + h_w$ and porosity at times 0, 1.25, 2.5, and 5 seconds (no interaction) [Colour figure can be viewed at wileyonlinelibrary.com]

The scheme is explicit, and we use a time step limit given by the CFL condition:

$$\Delta t_{SPH} \leq \frac{h_{\min}}{\left(\max\left(\sqrt{gh_I} + |v_I|\right)\right)} \tag{95}$$

In above equations, there is a term describing basal excess pore pressure at node I Δp_{wbI} which has to be obtained at each node and time step. One alternative is to use simple shape functions fulfilling boundary conditions at the surface and the basal surface. This has been used by Iverson and Denlinger[10] in 2001, Pastor and co-workers,[11,12,15,90] and Quecedo and coworkers.[20,21] This approach presents the limitation of not being able to model changes of boundary conditions at the bottom. For instance, when a landslide runs over a very permeable basal layer—or a rack—pore pressure becomes zero there, while in the body of the landslide is not zero. If a single shape function is used, once the basal value is set to zero, the pressure becomes zero in the whole depth.

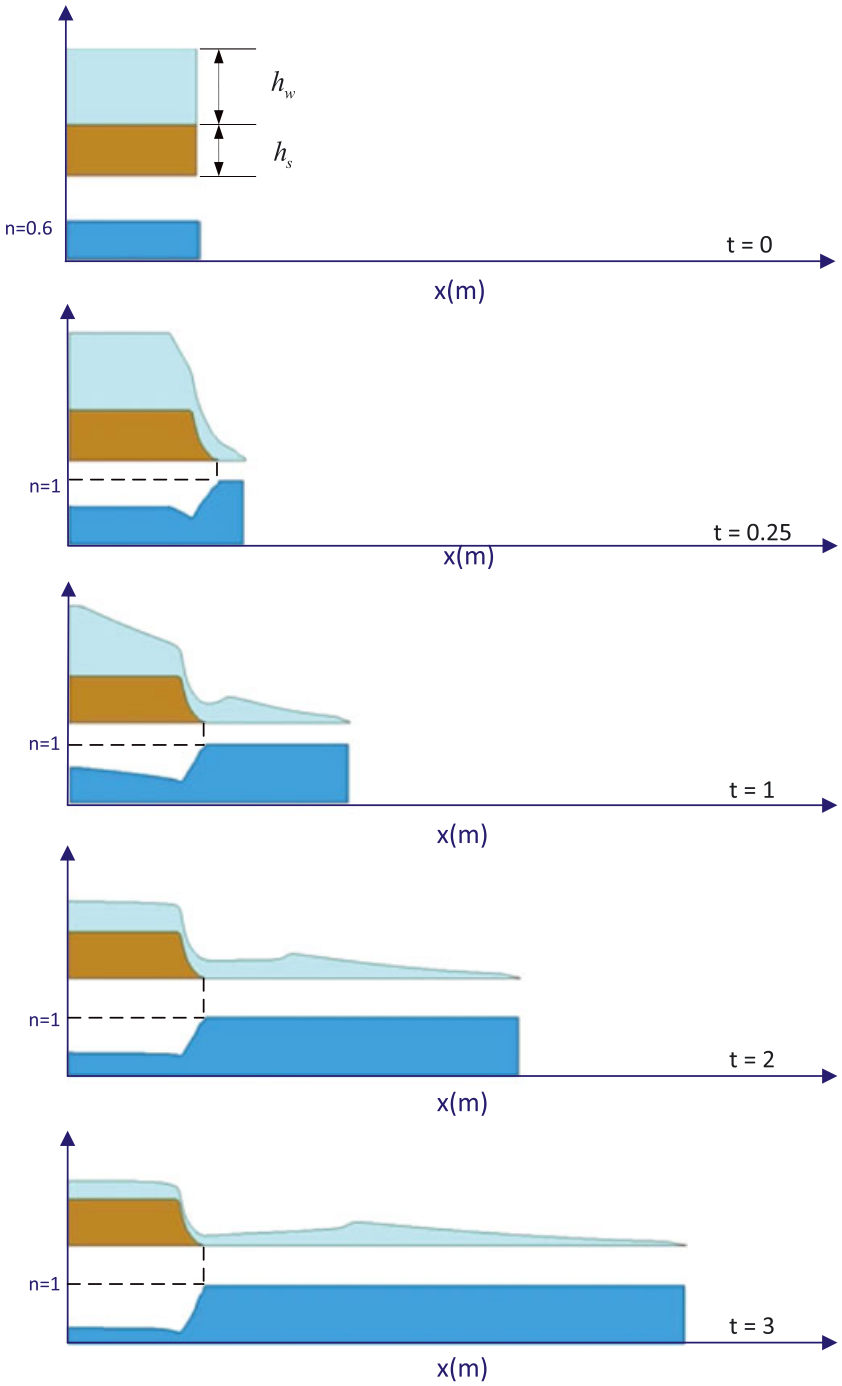

FIGURE 8 Profiles of h_s, $h_s + h_w$, and porosity n at times 0, 0.25, 1, 2, and 3 seconds (no interaction, friction angle 87°) [Colour figure can be viewed at wileyonlinelibrary.com]

Here, we will not consider excess pore pressures, which will be assumed to be zero. A variable smoothing length formula proposed in Benz[91] is considered in the present work.

$$h_I h_{SML\,I}^{NDIM} = const \tag{96}$$

where $h_{SML\,I}$ denotes the smoothing length at node I.

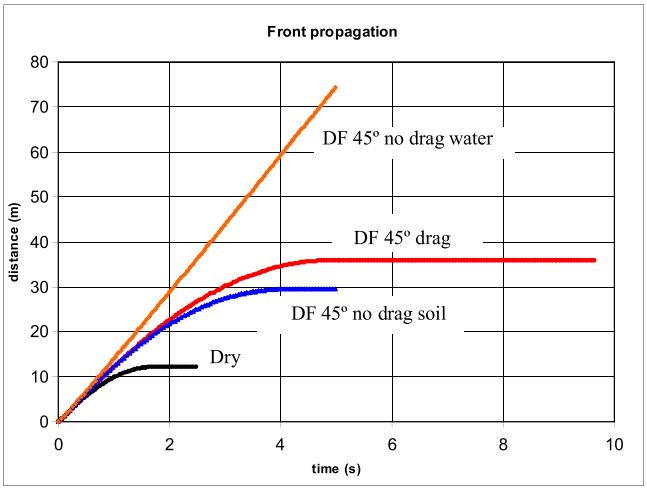

FIGURE 9 Front propagation for (1) dry material (2) mixture of soil and water with drag, (3) mixture without drag forces [Colour figure can be viewed at wileyonlinelibrary.com]

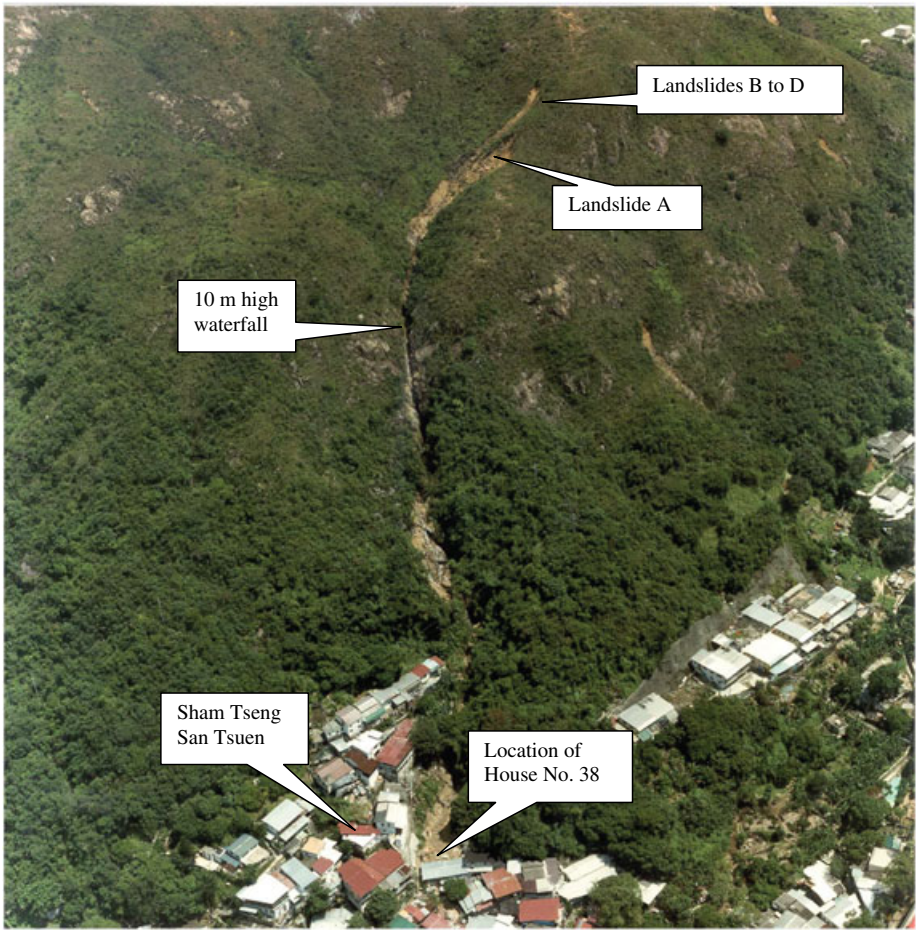

FIGURE 10 General view of the location (from Fugro Maunsell Scott Wilson Joint Venture[92] with permission) [Colour figure can be viewed at wileyonlinelibrary.com]

The algorithm is explicit and less accurate than the approach proposed by Bonet and co-workers[85] in 2004, where both the mass conservation equation and 96 were solved using a Newton Raphson algorithm.

So far, we have discretized the balance of mass 88 and the balance of momentum 93. The resulting equations are ODEs which can be integrated in time using a scheme such as Leap Frog or Runge Kutta (second or fourth order).

In the cases we will show in the section devoted to examples and applications, we have used a classical Runge Kutta fourth-order algorithm.

One important issue is the representation of the terrain over which the avalanche moves, as it greatly influences the results. If we denote by Z_I the height of the terrain at node I, we have to obtain (1) its gradient grad Z_I and (2) the radius of curvature along the tangent to the node path, which can be obtained from the second-order derivatives of Z.

In the case of fast landslides, the terrain information is given on a digital terrain model (DTM), which consists on a series of values (x_k, y_k, Z_k) at the nodes of a structured grid. From here, we can obtain both gradients and second derivatives at the grid nodes using a classical nodal recovery technique on a finite element mesh which nodes are those of the DTM grid.

Concerning the neighbor search, we have used an auxiliary structured grid covering the part of the terrain where the SPH particles are. Spacing is taken as the minimum smoothing length. For a given SPH node, search is restricted to the cell it belongs and its neighbors. This temporary grid is valid only for a given time step. In cases where the flow is elongated, the grid can be oriented automatically following the main inertia axes of the set of SPH nodes on the plane.

Finally, regarding boundary conditions of wall type, we have used a wall boundary condition in the first 2 examples which will be presented—the dams—but not in the practical application, as there were no walls nor obstacles. The method we have used consists of (1) defining the wall by a set of wall particles, (2) make zero the normal velocity to the wall if directed against it, and (3) normalize height of interacting nodes (see Equation 90).

4 | EXAMPLES AND APPLICATIONS

The purpose of this section is to illustrate the performance and limitations of the proposed 2-phase debris flow SPH model. Few are the papers published so far in this interesting topic. Following the work of Pitman and Le,[2] Pelanti and co-workers[90] and Pudasaini[3] continued the research, presenting interesting tests.

It is important to know that no analytical solution has been proposed so far for this problem, the tests presented by the authors mentioned above aiming to:

(i) Illustrate the mathematical features of the model
(ii) Simple tests showing the main features of the 2-phase model, comparing them to those of dry materials—or even with pure water.

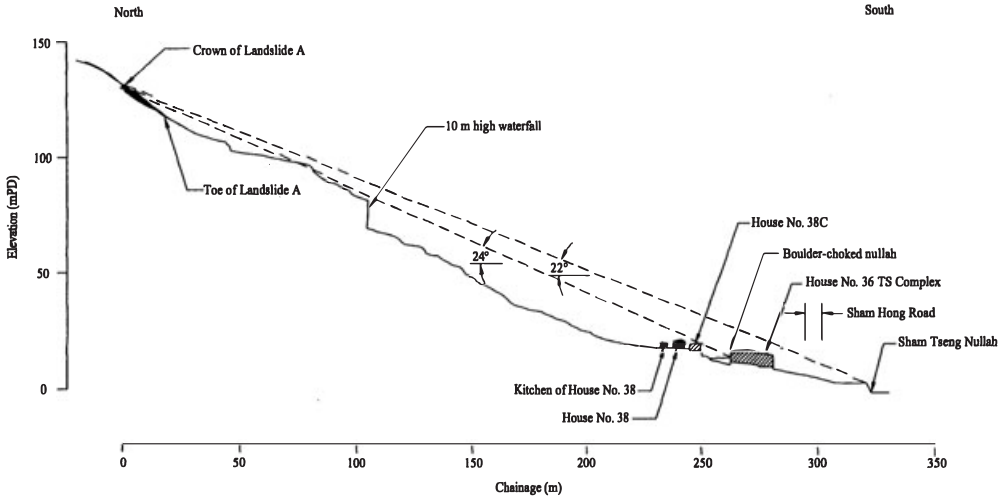

FIGURE 11 Elevation of debris flow path (from Fugro Maunsell Scott Wilson Joint Venture[92] with permission) [Colour figure can be viewed at wileyonlinelibrary.com]

We will go 1 step further, applying the model to a case of a real debris flow for which we have available information. The section is structured as follows:

(i) First of all, we will consider a thought experiment where a complex set of shocks and rarefaction waves appear.
(ii) Then, we will analyze the case of breaking of a dam impounding a mixture of granular material and water.
(iii) Finally, we will consider the case of Tseng San Tsuen debris flow,[91] which happened in Hong Kong.

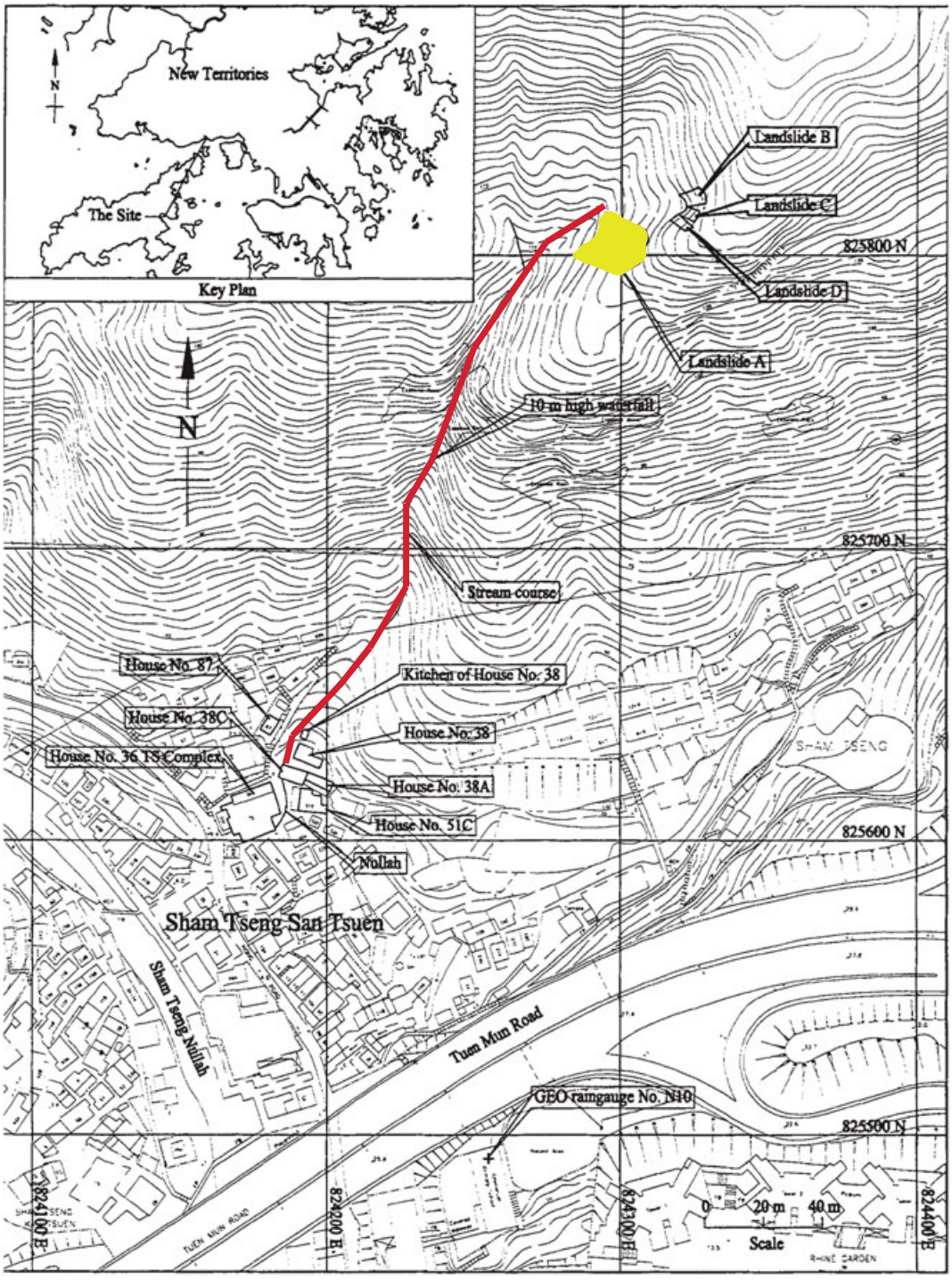

FIGURE 12 Terrain topography showing the debris flow track (from Fugro Maunsell Scott Wilson Joint Venture[92] with permission) [Colour figure can be viewed at wileyonlinelibrary.com]

4.1 | Shocks and expansion waves

The first example we will study is illustrated in Figure 2. It consists of a domain enclosed by 2 walls located at x = −10 m and x = 10 m filled with 2 masses having different heights and porosities:

$$h_L = 1.04\ h_{sL} = 0.32\ h_{wL} = 0.72\ n_L = 0.69$$
$$h_R = 1.38\ h_{sR} = 0.84\ h_{wR} = 0.54\ n_R = 0.39$$

We have depicted in the profile the total height $h = h_s + h_w$ and the height of the solid fraction h_s. The solid is assumed to have no strength, with particles of density $\rho_s = 2000\ Kg/m^3$ the water being inviscid. The interaction forces are given by Anderson formula,

$$R = -nR_w = (1-n)R_s$$
$$R = C_d(v_w - v_s)$$
$$C_d = \frac{n(1-n)}{V_T n^m}(\rho_s - \rho_w)g$$

where we have chosen $V_T = 1.e-3\ m/s\ \ m = 1$.

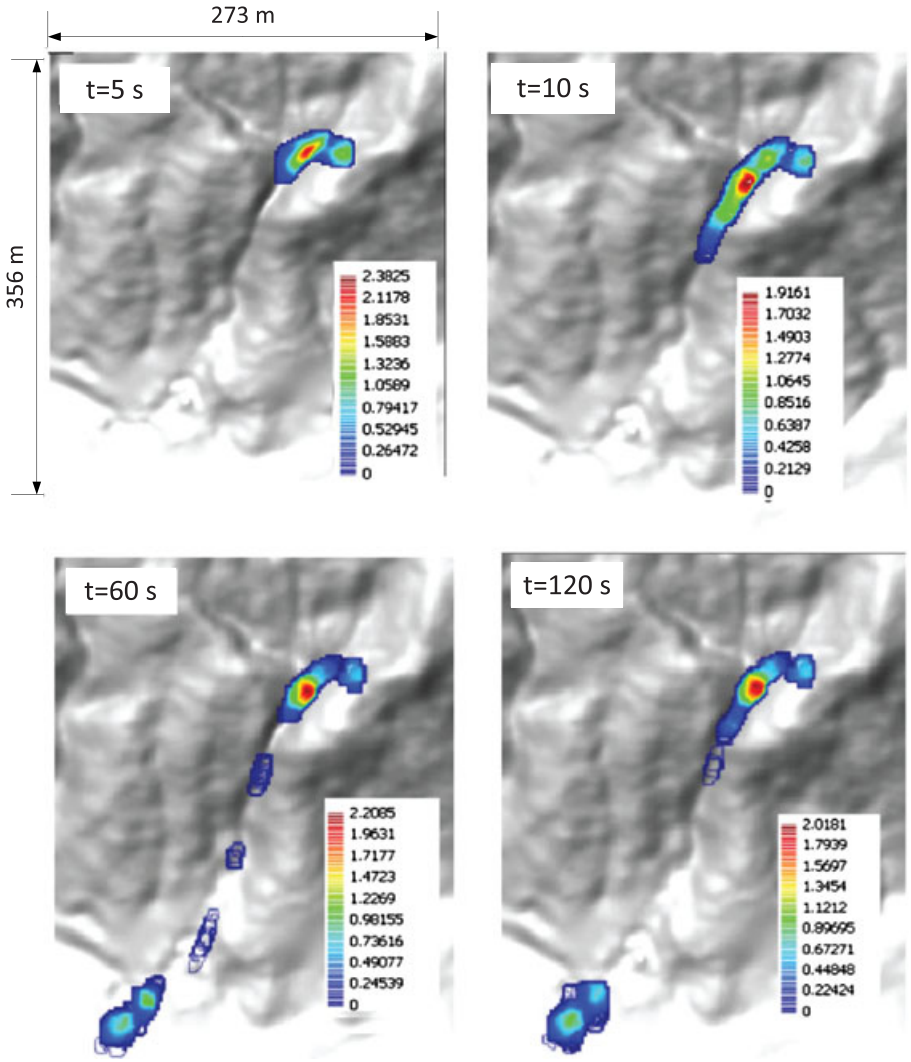

FIGURE 13 Terrain topography and profiles of debris flow height at times 5, 10, 60, and 120 seconds [Colour figure can be viewed at wileyonlinelibrary.com]

This test has been used in Pelanti et al[90] to show the complex pattern of rarefaction and shock waves in both solid and fluid phases. Debris flows having 2 phases with important relative mobility present a rich structure of shocks and rarefaction waves, which has to be properly modeled. Otherwise, the model will have numerical damping or dispersion.

At time zero, the wall separating both masses is removed. As soil and water have different heights, a complex pattern of shocks and rarefaction waves is produced. This is depicted in Figure 3, where we show the profiles of total height and soil fraction at times 0.5 , 1.0 , 1.5 , 2.0 , 3.5 , and 6 seconds.

Finally, we depict in Figure 4 the profiles of porosity at times 0 and 2 seconds.

4.2 | Breaking of a dam over a dry, horizontal basal surface

The second example we have selected is much more relevant, as it can be provide some insight on the propagation of 2-phase debris flows. The initial conditions are depicted in Figure 5.

Please note that we have assumed that the granular soil has a friction angle of 45°, the basal angle of friction being the same. The drag coefficients are the same used in the previous example.

The solution is depicted in Figure 6, where we provide the profiles of total height and soil fraction at times 0 , 1.25 , 2.5 , and 6 seconds.

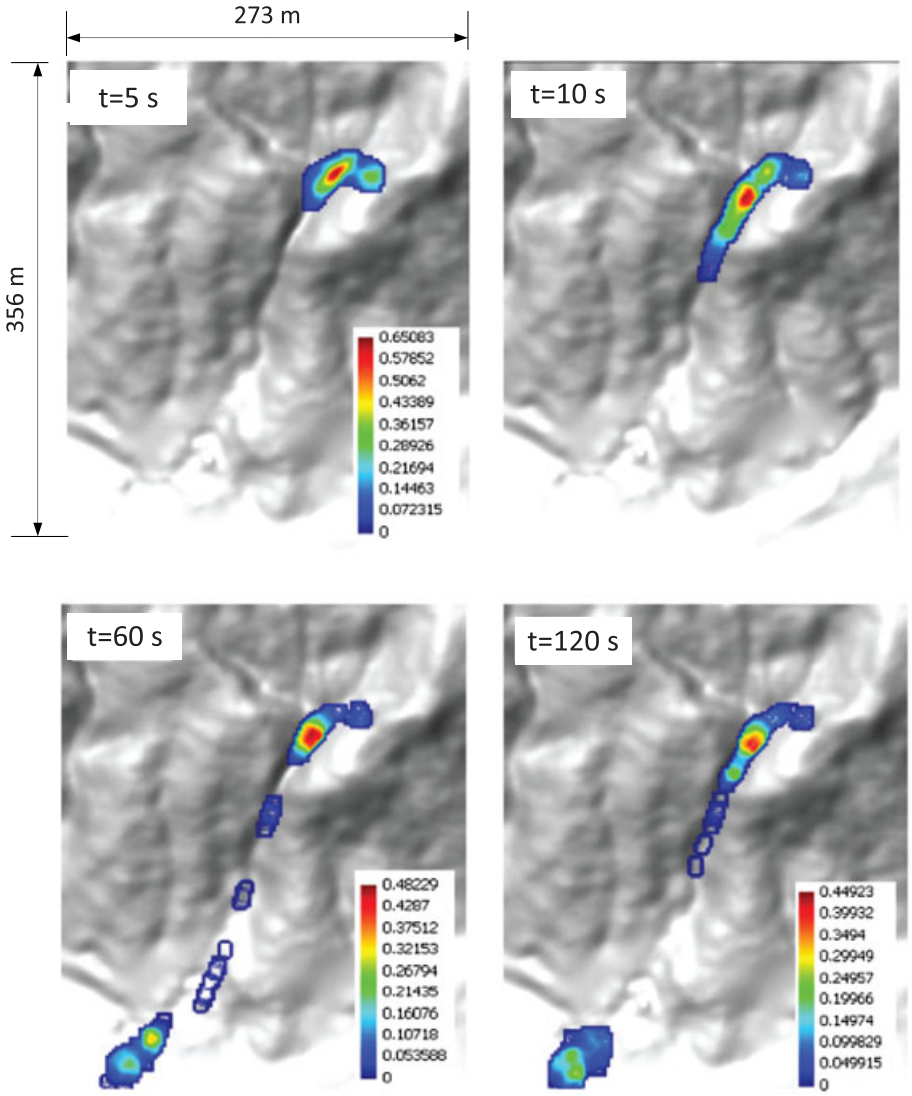

FIGURE 14 Terrain topography and profiles of h_w at times 5, 10, 60, and 120 seconds [Colour figure can be viewed at wileyonlinelibrary.com]

It is interesting to solve the same problem assuming that no interaction exists between solid and fluids. Results of total and solid phase heights together with the evolution of the porosity are shown in Figure 7. It is interesting to note how water abandons the solid.

We will present next in Figure 8 a limit case where we have modeled the solid choosing a tangent of the friction angle equal to 19, which is unrealistic, and we have not considered interaction between phases. This limit case represents a debris flow having a very high—unrealistic—friction angle, such that the solid grains stop while water leaves the skeleton, the interaction force not being able to mobilize the solid. In Figure 8, the total height together with that of the solid phase at times 0, 0.25, 1.0, 2.0, and 3.0 seconds can be observed. The evolution of the porosity is also shown in this figure.

Finally, we provide for all the dam break problems the propagation of the front along time. We have considered both of the cases described in this subsection, together with the case of a dry granular material in Figure 9.

Dambreak exercises provide interesting information in simple and controlled situations. We can see how both phases move relative to each other. From the simulations presented previously, we can see 3 cases of interest:

(i) That of a dry material, which presents the smallest runout (12 m)
(ii) The case of a mixture of soil grains—friction angle being 45°—and water, presenting a larger runout (35 m)
(iii) The case where interaction between phases is neglected. It can be observed how the solid phase stops (30 m) while the water continues flowing.

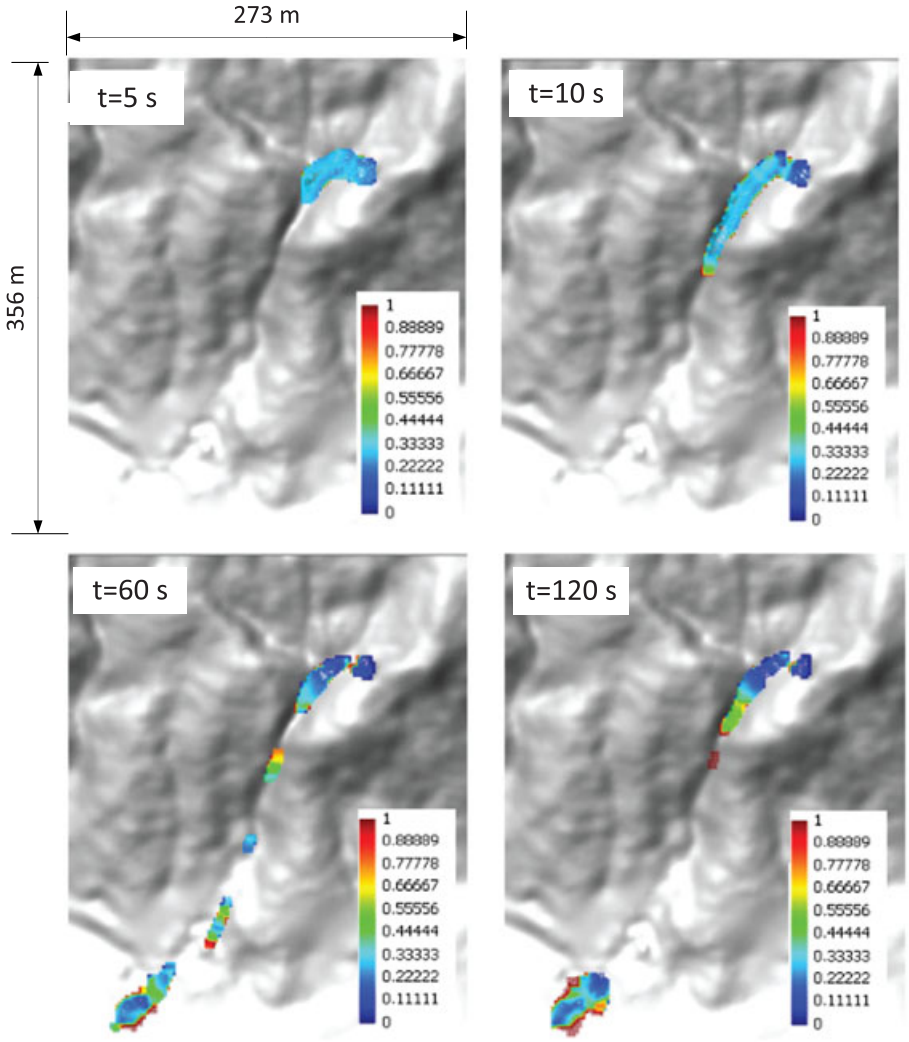

FIGURE 15 Terrain topography and profiles of porosity at times 5, 10, 60, and 120 seconds [Colour figure can be viewed at wileyonlinelibrary.com]

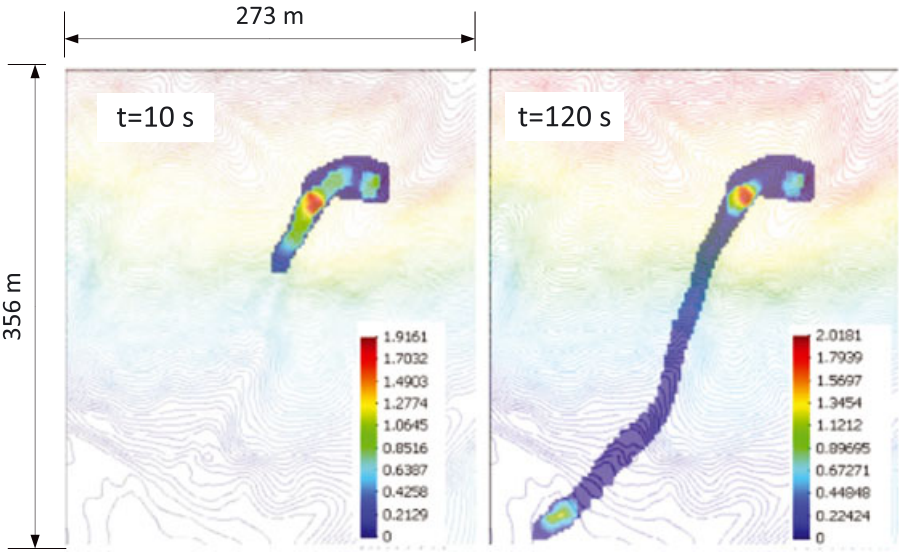

FIGURE 16 Terrain topography and path of debris flow showing profiles of $h = h_s + h_w$ at times 10 and 120 seconds [Colour figure can be viewed at wileyonlinelibrary.com]

4.3 | The Sham Tseng San Tsuen debris flow, Hong Kong

The debris flow we will consider here happened in Hong Kong on the 23rd of August 1999. This case is included in the set provided by Hong Kong Geotechnical Office, which in 2007 organized a benchmarking exercise aiming to assess the accuracy of numerical and constitutive models. The participants were provided a detailed digital terrain elevation map, including the original position of the mobilized mass and the final position of the deposit. The information can be found in Fugro Maunsell Scott Wilson.[92]

The event took place after an intense rainfall. Along the 24 hours before the event, rainfall was 479 mm. The debris flow consisted on 600 m^3 of channelized material, according to the report. It originated on 3 shallow landslides of which one was much larger than the others. Indeed, the data provided included only this main source. At the end of the channel, it destroyed a number of single storey buildings.

The picture from the data set is provided in Figure **10** displays the trail and the damaged buildings. Figure 11 provides a profile along the debris flow track, and Figure 12 depicts a terrain map where both the initial leading landslide and the track are shown.

From triaxial tests on the soils involved (loose to medium dense colluvium containing boulders and cobbles) and the CDG soils, it was concluded that cohesion was zero and the friction angle ranged from 37° to 38°, for which we find $\tan\phi' = 0.75 - 0.78$.

It is interesting to notice that, according to the report,[91] "... the distal end of the debris deposition had a travel angle of about 24°... ", much smaller than the friction angle found in laboratory tests. Moreover, in many models, it was proposed to use effective friction angles with $\tan\phi' = 0.35$, much smaller than that measured in laboratory.

In our analysis, we have assumed that friction angle is 31°. This value has been chosen as the one providing results close to those observed in the field. It is important to notice that propagation is a dynamic process, for which the triaxial results—valid for much lower strain rates—are not well known. Densities of soil particles, pore fluid, and mixture were taken as 2400 kg/m^3, 1000 kg/m^3, and 2000 kg/m^3. The drag law selected is the same described in the previous examples, with $V_T = 3.0e-2\, ms^{-1}$ $m = 1$.

We have used the data provided by Hong Kong Geotechnical Office, which included a digital terrain model including a layer with the initial mass. We concentrated on the propagation phase, the proposed model being not able to reproduce triggering. The initial heights ranged from 10 cm to 5 m approximately.

We present in Figure 13 the profile of $h = h_s + h_w$, in Figure 14, the profile of h_w, and in Figure 15, the profile of porosity at times 5, 10, 60, and 120 seconds.

Finally, the path of the debris flow is depicted in Figure 16 at times 10 and 120 seconds.

The discontinuities observed in the figures correspond to deposition of parts of the debris flows. The flow splits in several sections during the propagation, and we observe 2 deposition regions, on top and on the bottom.

5 | CONCLUSIONS

This paper has presented mathematical and numerical models which can be applied to reproduce the propagation of debris flows, taking into account coupling between solid and fluid phases. The mathematical model is based on those of Zienkiewicz and Shiomi,[1] Le and Pitman,[2] and Pudasaini.[3] The main assumption is that the height of the flowing material is fully occupied by both phases. Therefore, a material where only its lower part is saturated will not be considered here. The changes in porosities are a consequence of the relative movement of both phases, without any extra pore pressure being generated.

The numerical models are of lagrangian type (SPH). We propose to use a double set of nodes (solid and fluid) which can move relatively to each other. The drag depends on the relative velocity between phases. It is possible to find situations where the fluid abandons the body of the mixture using 2 set of nodes.

The rheological model used is of frictional type, without additional turbulent viscosity terms of Voellmy type, for instance. The fluid has been assumed inviscid, which is a crude approximation of cases where it contains fine particles. It is interesting to notice that the friction angles used are realistic, being close of those measured in triaxial tests.

The set of tests presented includes examples where we illustrate:

(i) The complex set of shock and rarefaction waves which can be produced in some cases.
(ii) The difference of behavior between dry materials and debris flows.
(iii) The possibility of a water abandoning the main mass.
(iv) A real case that happened in Hong Kong.

ACKNOWLEDGEMENTS

The authors gratefully acknowledge the economic support provided by the Spanish Ministry MINECO under projects GEOFLOW (BIA2012-37020-C02-01) and ALAS (BIA2016-76253-P). In addition, the authors gratefully acknowledge the support of the Geotechnical Engineering Office, Civil Engineering, and Development Department of the Government of the Hong Kong SAR in the provision of the digital terrain models for the Hong Kong landslide cases.

ORCID

A. Yague http://orcid.org/0000-0002-3290-9433
M.M. Stickle http://orcid.org/0000-0001-7591-418X
D. Manzanal http://orcid.org/0000-0002-6087-3255

REFERENCES

1. Zienkiewicz OC, Shiomi T. Dynamic behaviour of saturated porous media: the generalized biot formulation and its numerical solution. *Int J Numer Anal Methods Geomech.* 1984;8:71-96.
2. Pitman EB, Le L. A two-fluid model for avalanche and debris flows. *Philos Trans A Math Phys Eng Sci.* 2005;363:1573-1601.
3. Pudasaini SP. A general two-phase debris flow model. *J Geophys Res.* 2012;117:F03010
4. Dikau R, Commission E. *Landslide Recognition: Identification, Movement, and Causes.* New York: John Wiley & Sons; 1996.
5. Hutchinson JN. Morphological and geotechnical parameters of landslides in relation to geology and hydrogeology. Proc. 5th International Symposium on Landslides. Lausanne, 1988. Vol. VI: 3–35. A. A. Balkema Publ. Rotterdam, 1988.
6. Biot MA. General theory of three-dimensional consolidation. *J Appl Phys.* 1941;12:155-164.
7. Biot MA. Theory of elasticity and consolidation for a porous anisotropic solid. *J Appl Phys.* 1955;26:182-185.
8. Bowen RM. In: Eringen AC, ed. *Theory of Mixtures, Part I. Continuum Physics III.* New York: Academic Press; 1976.
9. Anderson TB, Jackson R. Fluid mechanical description of fluidized beds. Equations of motion. *Ind Eng Chem Fundam.* 1967;6(4):527-539.
10. Iverson RM, Denlinger RP. Flow of variably fluidized granular masses across three-dimensional terrain: 1. Coulomb mixture theory. *J Geophys.* 2001;106:537-552.
11. Pastor M, Quecedo M, Fernández Merodo JA, Herreros MI, Gonzalez E, Mira P. Modelling tailings dams and mine waste dumps failures. *Géotechnique.* 2002;52:579-591.

12. Pastor M, Haddad B, Sorbino G, Cuomo S, Drempetic V. A depth-integrated, coupled SPH model for flow-like landslides and related phenomena. *Int J Numer Anal Methods Geomech.* 2009;33:143-172.
13. Prime N, Dufour F, Darve F. Unified model for geomaterial solid/fluid states and the transition in between. *J Eng Mech*. 2013;140(6): 04014031
14. Berzi D, Di Prisco CG, Vescovi D. Constitutive relations for steady, dense granular flows. *Phys Rev E*. 2011;84(3): 031301
15. Pastor M, Stickle MM, Dutto P, et al. A viscoplastic approach to the behaviour of fluidized geomaterials with application to fast landslides. *Continuum Mechanics and Thermodynamics*. 2015;27:21-47.
16. Pastor M, Blanc T, Haddad B, et al. Depth averaged models for fast landslide propagation: mathematical, rheological and numerical aspects. *Archives of Computational Methods in Engineering*. 2015;22:67-104.
17. Blanc T, Pastor M. A stabilized fractional step, Runge–Kutta Taylor SPH algorithm for coupled problems in geomechanics. *Comput Methods Appl Mech Eng*. 2012;221-222:41-53.
18. Blanc T, Pastor M. A stabilized smoothed particle hydrodynamics, Taylor–Galerkin algorithm for soil dynamics problems. *International Journal for Numerical and Analytical Methods in Geomechanics*. 2013;37(1):1-30.
19. Quecedo M, Pastor M. Application of the level set method to the finite element solution of two-phase flows. *Int J Numer Methods Eng*. 2001;50(3):645-663.
20. Quecedo M, Pastor M, Herreros MI. Numerical modelling of impulse wave generated by fast landslides. *Int J Numer Methods Eng*. 2004;59(12):1633-1656.
21. Quecedo M, Pastor M, Herreros MI, Fernández Merodo JA. Numerical modelling of the propagation of fast landslides using the finite element method. *Int J Numer Methods Eng*. 2004;59:755-794.
22. McDougall S, Hungr O. A model for the analysis of rapid landslide motion across three-dimensional terrain. *Canadian Geotechnical Journal*. 2004;41(6):1084-1097.
23. Rodriguez-Paz M, Bonet J. A corrected smooth particle hydrodynamics formulation of the shallow-water equations. *Comput Struct.* 2005;83:1396-1410.
24. Zienkiewicz OC, Chan AHC, Pastor M, Shrefler BA, Shiomi T. *Computational Geomechanics with Special Reference to Earthquake Engineering*. New York: John Wiley & Sons; 1999.
25. Lewis RW, Schrefler BA. *The Finite Element Method in the Static and Dynamic Deformation and Consolidation of Porous Media*. Chichester, UK: JohnWiley &Sons; 1998.
26. Zienkiewicz OC, Chan AHC, Pastor M, Paul DK, Shiomi T. Static and dynamic behaviour of soils: a rational approach to quantitative solutions. I. Fully saturated problems. *Proc R Soc Lond.* 1877;1990(429):285-309.
27. Zienkiewicz OC, Xie YM, Schrefler BA, Ledesma A, Bicanic N. Static and dynamic behaviour of soils: a rational approach to quantitative solutions. II. Semi-saturated problems. *Proc R Soc Lond*. 1877;1990(429):311-321.
28. Fernández Merodo JA, Pastor M, Mira P, et al. Modelling of diffuse failure mechanisms of catastrophic landslides. *Comp Methods Appl Mech Engrg*. 2004;193:2911-2939.
29. Saint-Venant A. Theorie du mouvement non permanent des eaux, avec application aux crues des rivieres et a l'introduction de marees dans leurs lits. *Comptes-Rendus l'Académie des Sci*. 1871;73:147-273.
30. Savage SB, Hutter K. The dynamics of avalanches of granular materials from initiation to runout. Part I: analysis. *Acta Mech.* 1991;86:201-223.
31. Hutter K, Koch T. Motion of a granular avalanche in an exponentially curved chute: experiments and theoretical predictions. *Philos Trans R Soc A Math Phys Eng Sci*. 1991;334:93-138.
32. Hutter K, Siegel M, Savage SB, Nohguchi Y. Two-dimensional spreading of a granular avalanche down an inclined plane part I. Theory. *Acta Mech*. 1993;100:37-68.
33. Gray JMNT, Wieland M, Hutter K. Gravity-driven free surface flow of granular avalanches over complex basal topography. *Proc R Soc A Math Phys Eng Sci*. 1999;455:1841-1874.
34. Laigle D, Coussot P. Numerical modeling of mudflows. *J Hydraul Eng*. 1997;123:617-623.
35. Pastor M, Blanc T, Pastor MJ. A depth-integrated viscoplastic model for dilatant saturated cohesive-frictional fluidized mixtures: application to fast catastrophic landslides. *Journal of Non-Newtonian Fluid Mechanics*. 2009;158(1):142-153.
36. Pudasaini SP, Hutter K. *Avalanche Dynamics: Dynamics of Rapid Flows of Dense Granular Avalanches*. London: Springer; 2007.
37. Hutter K, Wang Y, Pudasaini SP. The Savage-Hutter avalanche model: how far can it be pushed? *Phil Trans R Soc A*. 2005;363:1507-1528.
38. Hutchinson JN. A sliding–consolidation model for flow slides. *Can Geotech J*. 1986;23:115-126.
39. Iverson RI. The physics of debris flows. *Rev Geophys*. 1997;35:245-296.
40. Wang Y, Hutter K. A constitutive theory of fluid-saturated granular materials and its application in gravitational flows. *Rheol Acta*. 1999;38:214-223.

41. Hungr O, McDougall S, Bovis M. Debris flow hazard and related phenomena, chapter 7. In: Jakob M, Hungr O, eds. *Entrainment of Material by Debris Flows*. Berlin: Springer and Praxis; 2005:135-158.

42. Nayroles B, Touzot G, Villon P. Generalizing the finite element method: diffuse approximation and diffuse elements. *Comput Mech*. 1992;10:307-318.

43. Belytschko T, Lu YY, Gu L. Element-free Galerkin methods. *Int J Numer Methods Eng*. 1994;37:229-256.

44. Duarte CA, Oden JT. An h-p adaptive method using clouds. *Comput Methods Appl Mech Eng*. 1996;139:237-262.

45. Melenk JM, Babuška I. The partition of unity finite element method: basic theory and applications. *Comput Methods Appl Mech Eng*. 1996;139:289-314.

46. Oñate E, Idelsohn S. A mesh-free finite point method for advective-diffusive transport and fluid flow problems. *Comput Mech*. 1998;21:283-292.

47. Salazar F, Oñate E, Morán R. Numerical modeling of landslides in reservoirs using the particle finite element method (PFEM). Proceedings of the 3rd International Forum on Risk Analysis, Dam Safety, Dam Security, and Critical Infrastructure Management 2011: 245–250.

48. Więckowski Z. The material point method in large strain engineering problems. *Comput Methods Appl Mech Eng*. 2004;193:4417-4438.

49. Coetzee CJ, Vermeer PA, Basson AH. The modelling of anchors using the material point method. *Int J Numer Anal Methods Geomech*. 2005;29:879-895.

50. Andersen S, Andersen L. Modelling of landslides with the material-point method. *Comput Geosci*. 2010;14:137-147.

51. Zabala F, Alonso E. Progressive failure of Aznalcóllar dam using the material point method. *Géotechnique*. 2011;61:795-808.

52. Jassim I, Stolle D, Vermeer P. Two-phase dynamic analysis by material point method. *Int J Numer Anal Methods Geomech*. 2013;37:2502-2522.

53. Lucy LB. A numerical approach to the testing of the fission hypothesis. *Astron J*. 1977;82:1013

54. Gingold RA, Monaghan JJ. Smoothed particle hydrodynamics—theory and application to non-spherical stars. *Mon Not R Astron Soc*. 1977;375-389.

55. Monaghan JJ, Kos A. Solitary waves on a Cretan Beach. *J Waterw Port, Coastal, Ocean Eng*. 1999;125:145-155.

56. Zhu Y, Fox PJ. Smoothed particle hydrodynamics model for diffusion through porous media. *Transp Porous Media*. 2001;43:441-471.

57. Ata R, Soulaïmani A. A stabilized SPH method for inviscid shallow water flows. *Int J Numer Methods Fluids*. 2005;47:139-159.

58. Vacondio R, Rogers BD, Stansby PK, Mignosa P, Feldman J. Variable resolution for SPH: a dynamic particle coalescing and splitting scheme. *Comput Methods Appl Mech Eng*. 2013;256:132-148.

59. Vacondio R, Mignosa P, Pagani S. 3D SPH numerical simulation of the wave generated by the Vajont rockslide. *Adv Water Resour*. 2013;59:146-156.

60. Vacondio R, Rogers BD, Stansby PK, Mignosa P. Shallow water SPH for flooding with dynamic particle coalescing and splitting. *Adv Water Resour*. 2013;58:10-23.

61. Xia X, Liang Q, Pastor M, Zou W, Zhuang YF. Balancing the source terms in a SPH model for solving the shallow water equations. *Adv Water Resour*. 2013;59:25-38.

62. Liu GR, Liu MB. *Smoothed Particle Hydrodynamics: A Meshfree Particle Method*. World Scientific; 2003.

63. Li S, Liu WK. *Meshfree particle methods*. Berlin: Springer; 2004.

64. Libersky LD, Petschek AG. Smooth particle hydrodynamics with strength of materials. Advances in the Free-Lagrange Method Including Contributions on Adaptive Gridding and the Smooth Particle Hydrodynamics Method. Berlin; 1991: 248–257.

65. Libersky LD, Petschek AG, Carney TC, Hipp JR, Allahdadi FA. High strain Lagrangian hydrodynamics. *J Comput Phys*. 1993;109:67-75.

66. Randles PW, Libersky LD. Smoothed particle hydrodynamics: some recent improvements and applications. *Comput Methods Appl Mech Eng*. 1996;139:375-408.

67. Randles PW, Libersky LD. Normalized SPH with stress points. *Int J Numer Methods Eng*. 2000;48:1445-1462.

68. Bonet J, Kulasegaram S. Correction and stabilization of smooth particle hydrodynamics methods with applications in metal forming simulations. *Int J Numer Methods Eng*. 2000;47:1189-1214.

69. Gray JP, Monaghan JJ, Swift RP. SPH elastic dynamics. *Comput Methods Appl Mech Eng*. 2001;190:6641-6662.

70. Bui HH, Sako K, Fukagawa R. Numerical simulation of soil–water interaction using smoothed particle hydrodynamics (SPH) method. *J Terramechanics*. 2007;44:339-346.

71. Bui HH, Fukagawa R, Sako K, Ohno S. Lagrangian meshfree particles method (SPH) for large deformation and failure flows of geomaterial using elastic-plastic soil constitutive model. *Int J Numer Anal Methods Geomech*. 2008;32:1537-1570.

72. Blanc T, Pastor M. A stabilized Runge-Kutta, Taylor smoothed particle hydrodynamics algorithm for large deformation problems in dynamics. *Int J Numer Methods Eng*. 2012;91:1427-1458.

73. Monaghan J, Gingold R. Shock simulation by the particle method SPH. *J Comput Phys*. 1983;52:374-389.

74. Monaghan JJ, Lattanzio JC. A refined particle method for astrophysical problems. *Astron Astrophys*. 1985;149:135-143.

75. Morris JP. Analysis of smoothed particle hydrodynamics with applications. Monash University. PhD Thesis. Australia, 1996.

76. Chen JK, Beraun JE, Carney TC. A corrective smoothed particle method for boundary value problems in heat conduction. *Int J Numer Methods Eng*. 1999;46:231-252.

77. Swegle JW, Hicks DL, Attaway SW. Smoothed particle hydrodynamics stability analysis. *J Comput Phys*. 1995;116:123-134.

78. Monaghan JJ. SPH without a tensile instability. *J Comput Phys*. 2000;159:290-311.

79. Dyka CT, Ingel RP. An approach for tension instability in smoothed particle hydrodynamics (SPH). *Comput Struct*. 1995;57:573-580.

80. Dyka CT, Randles PW, Ingel RP. Stress points for tension instability in SPH. *Int J Numer Methods Eng*. 1997;40:2325-2341.

81. Peraire J, Zienkiewicz OC, Morgan K. Shallow water problems: a general explicit formulation. *Int J Numer Methods Eng*. 1986;22:547-574.

82. Donea J, Giuliani S, Laval H, Quartapelle L. Time-accurate solution of advection-diffusion problems by finite elements. *Comput Methods Appl Mech Eng*. 1984;45:123-145.

83. Mabssout M, Pastor M. A Taylor–Galerkin algorithm for shock wave propagation and strain localization failure of viscoplastic continua. *Comput Methods Appl Mech Eng*. 2003;192:955-971.

84. Monaghan JJ. Why particle methods work. *SIAM J Sci Stat Comput*. 1982;3:422-433.

85. Bonet J, Kulasegaram S, Rodriguez-Paz MX, Profit M. Variational formulation for the smooth particle hydrodynamics (SPH) simulation of fluid and solid problems. *Comput Methods Appl Mech Eng*. 2004;193:1245-1256.

86. Lastiwka M, Quinlan N, Basa M. Adaptive particle distribution for smoothed particle hydrodynamics. *Int J Numer Methods Fluids*. 2005;47:1403-1409.

87. Vacondio R, Rogers BD, Stansby PK, Mignosa P. SPH modeling of shallow flow with open boundaries for practical flood simulation. *J Hydraul Eng*. 2012;138:530-541.

88. Monaghan JJ. Particle methods for hydrodynamics. *Comput Phys Reports*. 1985;3:71-124.

89. Monaghan JJ. Smoothed particle hydrodynamics. *Annu Rev Astron Astrophys*. 1992;30:543-574.

90. Pelanti M, Bouchut F, Mangeney A. A roe-type scheme for two-phase shallow granular flows over variable topography. *Math Model Numer Anal*. 2008;42:851-885.

91. Benz W. Smooth particle hydrodynamics—a review. Proceedings of the NATO Advanced Research Workshop on The Numerical Modelling of Nonlinear Stellar Pulsations Problems and Prospects, 1990: 269.

92. Fugro Maunsell Scott Wilson Joint Venture. Report on the debris flow at Sham Tseng San Tsuen of 23 August 1999. Findings of the investigation. GEO REPORT No. 169, Geotechnical Engineering Office, Civil Engineering and Development Department, The Government of the Hong Kong Special Administrative Region, 2005.

How to cite this article: Pastor M, Yague A, Stickle MM, Manzanal D, Mira P. A two-phase SPH model for debris flow propagation. *Int J Numer Anal Methods Geomech*. 2017;1–31. https://doi.org/10.1002/nag.2748